Journal of Hematology & Oncology

RESEARCH

Open Access

Novel potent molecular glue degraders against broad range of hematological cancer cell lines via multiple neosubstrates degradation

Pengyun Li[1,2†], Xiaotong Hu[1,2†], Zhiya Fan[3†], Shiyang Sun[1,2], Qijie Ran[4,5], Ting Wei[1,2], Pengli Wei[1,2], Qiyu Jiang[4], Jian Yan[1,2], Ning Yang[1,2], Changkai Jia[1,2], Tingting Yang[6], Yaqiu Mao[1,2], Xu Cai[1,2], Tingting Xu[1,2], Zhiyuan Zhao[1,2], Xiaohong Qian[3], Weijie Qin[3], Xiaomei Zhuang[2*], Feng Fan[4*], Junhai Xiao[1,2*], Zhibing Zheng[1,2*] and Song Li[1,2]

Abstract

Background Targeted protein degradation of neosubstrates plays a crucial role in hematological cancer treatment involving immunomodulatory imide drugs (IMiDs) therapy. Nevertheless, the persistence of inevitable drug resistance and hematological toxicities represents a significant obstacle to their clinical effectiveness.

Methods Phenotypic profiling of a small molecule compounds library in multiple hematological cancer cell lines was conducted to screen for hit degraders. Molecular dynamic-based rational design and cell-based functional assays were conducted to develop more potent degraders. Multiple myeloma (MM) tumor xenograft models were employed to investigate the antitumor efficacy of the degraders as single or combined agents with standard of care agents. Unbiased proteomics was employed to identify multiple therapeutically relevant neosubstrates targeted by the degraders. MM patient-derived cell lines (PDCs) and a panel of solid cancer cell lines were utilized to investigate the effects of candidate degrader on different stage of MM cells and solid malignancies. Unbiased proteomics of IMiDs-resistant MM cells, cell-based functional assays and RT-PCR analysis of clinical MM specimens were utilized to explore the role of BRD9 associated with IMiDs resistance and MM progression.

Results We identified a novel cereblon (CRBN)-dependent lead degrader with phthalazinone scaffold, **MGD-4**, which induced the degradation of Ikaros proteins. We further developed a novel potent candidate, **MGD-28**, significantly

†Pengyun Li, Xiaotong Hu and Zhiya Fan contributed equally to this work.

*Correspondence:
Xiaomei Zhuang
xiaomeizhuang@163.com
Feng Fan
fengfanbio@126.com
Junhai Xiao
xiaojunhai@139.com
Zhibing Zheng
zzbcaptain@aliyun.com

Full list of author information is available at the end of the article

inhibited the growth of hematological cancer cells and induced the degradation of IKZF1/2/3 and CK1α with nanomolar potency via a Cullin-CRBN dependent pathway. Oral administration of **MGD-4** and **MGD-28** effectively inhibited MM tumor growth and exhibited significant synergistic effects with standard of care agents. **MGD-28** exhibited preferentially profound cytotoxicity towards MM PDCs at different disease stages and broad antiproliferative activity in multiple solid malignancies. BRD9 modulated IMiDs resistance, and the expression of BRD9 was significant positively correlated with IKZF1/2/3 and CK1α in MM specimens at different stages. We also observed pronounced synergetic efficacy between the BRD9 inhibitor and **MGD-28** for MM treatment.

Conclusions Our findings present a strategy for the multi-targeted degradation of Ikaros proteins and CK1α against hematological cancers, which may be expanded to additional targets and indications. This strategy may enhance efficacy treatment against multiple hematological cancers and solid tumors.

Keywords Hematological cancer, Molecular glue, IMIDs, Cereblon, Rational drug design, Neosubstrate, Drug resistance

Background

Targeted protein degradation in recent decades has emerged as a revolutionary therapeutic strategy in oncology. Prototypical immunomodulatory imide drugs (IMiDs) including thalidomide, lenalidomide, and pomalidomide, are widely used in the treatment of various hematological cancers such as multiple myeloma (MM), acute myeloid leukemia (AML), and diffuse large B cell lymphoma (DLBCL) [1–3]. These IMiDs function as molecular glues by binding to cereblon (CRBN), the substrate receptor of the CRL4 E3 ubiquitin ligase and induce the formation of a composite protein-small molecule surface, which alters the specificity of the complex and leads to the recruitment, polyubiquitination, and subsequent degradation of proteins (neosubstrates) by the 26S proteasome [4]. The Ikaros family of zinc finger transcription factors, specifically the three reported members, IKZF1, IKZF2, and IKZF3, play pivotal roles in hematological development and differentiation. Initially, IKZF1 and IKZF3 were identified as neosubstrates of IMiDs, which may explain the clinical effectiveness of lenalidomide and pomalidomide in the treatment of MM [5, 6]. In mouse syngeneic tumor models, IKZF2 enhances the secretion of proinflammatory cytokines and promotes an anti-tumor immune response. In the past decade, numerous neosubstrates have been demonstrated to be degraded by IMiDs or their derivatives, and to participate in their pharmacological mechanism. These neosubstrates include casein kinase 1α (CK1α) [7], ZFP91 [8], GSPT1 [9], DTWD1 [10], SALL4 [11], ZBTB16 [12], p63 [13], ZMYM2 [14], RAB28 and RNF166 [10], highlighting a burgeoning therapeutic approach. It is noteworthy that several next-generation CRBN modulators are being developed to treat various hematological malignancies, including CC-220, CC-99282, CC-92480, and CFT7455 are IKZF1/3 degraders, and DYK709 is an IKZF2 degrader [4]. Nevertheless, most of these degraders are developed merely by extending the structure of prototypical IMiDs to optimize druggability. Additionally, these agents exhibited ubiquitous hematological toxicity in preclinical and clinical studies [1]. Although several promising targeted therapies, including proteasome inhibitors, oral immunomodulatory agents, and dexamethasone followed by autologous hematopoietic stem cell transplantation, are considered standard treatments for patients with MM, and the use of FLT-3 inhibitors, BCL-2 inhibitors, IDH2 inhibitors and their combination with azacytidine or decitabine has led to great advances in the treatment of AML, therapy resistance remains a significant challenge, as it results in the emergence of different clones at diagnosis and relapse [15, 16]. Consequently, the development of novel degraders for multiple neosubstrates with low toxicity represents a promising avenue for exploring therapeutic opportunities to treat various hematological malignancies.

CK1α is a ubiquitously expressed cytosolic serine/threonine kinase involved in the regulation of the Wnt/β-catenin and p53 signaling pathways. Previous studies demonstrated the pivotal role of CK1α in the survival of AML cells, both in vitro and in vivo. Degradation of CK1α provides a mechanistic explanation for the unique clinical effectiveness of lenalidomide in myelodysplastic syndrome (MDS) patients with deletion of chromosome 5q (del(5q)) [7, 17]. Silencing of CK1α, using short interfering RNA against CSNK1A1 enhances apoptosis and growth arrest induced by lenalidomide in NCI-H929 cells. In addition, inhibition of CK1α activates the pro-apoptotic effect of p53-MDMX and promotes myeloid differentiation in AML [18]. Furthermore, CK1α enhances the survival of lymphoma cells and a range of solid tumors, including lung, renal, and colorectal cancers [19, 20]. To date, lenalidomide is the only FDA-approved drug known to induce degradation of CK1α protein, albeit weakly [7]. Recent studies reported the development of selective CK1α degraders and dual CK1α/IKZF2 degraders through elegant medicinal chemistry efforts [21, 22]. These findings suggest that a

more effective CK1α degrader could exhibit even greater potency and broader clinical anticancer applications.

Several studies revealed distinct patterns of substrate specificity among various IMiDs. Both pomalidomide and lenalidomide were shown to degrade the transcription factor IKZF1/3, whereas neither drug degrades IKZF2. Furthermore, lenalidomide targets CK1α to CRBN, whereas pomalidomide does not [23]. This evidence underscores the structural basis that ligand modification can affect the interaction between neosubstrates and the CRBN interface, and also supports the hypothesis that structural modifications of ligands can diversify neosubstrate targeting, extending beyond traditionally known targets. In this study, we used an exclusive molecule glue compound library consisting of various CRBN ligands with novel scaffolds to conduct cell-based phenotypic screening in a range of hematological cancer cell lines. Through subsequent exploration of structure-activity relationships and protein degradation mechanisms, we identified novel degraders that effectively target Ikaros proteins and CK1α. These highly potent, selective, and orally bioavailable degraders could serve as promising candidates for further research and development.

Materials and methods

General chemical information

All regents and solvents were purchased from commercially available sources and were used without further purification. All reactions were conducted under appropriate pressure and temperature in glassware that had been oven-dried prior to use. Thin-layer chromatography (TLC) was performed using precoated silica gel plates from Qingdao Haiyang Chemical Co. Flash column chromatography was performed with the silica gel (particle size of 40–63 μm). ^{1}H and ^{13}C nuclear magnetic resonance (NMR) spectra were recorded on Bruker AVANCE NEO 600 MHz (operating at 600 MHz for ^{1}H and 151 MHz for ^{13}C acquisitions) and JNM-ECZ400S spectrometers. High-resolution mass spectra Analysis were obtained on AB Sciex API 3000™ LC/MS.

Biological assays

Reagents

Thalidomide (#T0213), pomalidomide (#T2384), lenalidomide (#T1642), CC-122 (#T3549), CC-220 (#T7791), CC-885 (#T14893), MLN4924 (#6332), dexamethasone (#T1076), tazemetostat (#T1788) and bortezomib (#T2399) were purchased from Targetmol, Boston, MA, USA. Cycloheximide (#S7418) was purchased from Selleck, Houston, TX, USA. The synthesis and characterization of molecular glue degraders in this study are described in Supplementary Information. All drugs were dissolved in dimethylsulfoxide (DMSO, #D8418; Sigma-Aldrich, MO, USA) at 10-200 mM, stored at -30 °C as stock solutions.

Plasmids

The pcDNA3.1(+) plasmids were purchased from Invitrogen, Carlsbad, CA, USA. The open reading frames (ORFs) of IKZF1, IKZF2, IKZF3, $CK1\alpha^{WT}$ and $CK1\alpha^{G40N}$ were amplified, and restriction enzyme sites were added by PCR and cloned into pcDNA3.1(+)-AGIA-MCS. The primers used in PCR experiments were available in Table S1

Cell culture and transfection

HEK293T (#CRL-3216) cells were cultured in high-glucose Dulbecco's modified Eagle's medium (DMEM, #SH30022.01; Hyclone, Logan, UT, USA). MM cell lines including RPMI-8226, NC-H929, OPM-2, and AML cell lines including U937, MOLM-13, and Ocl-Ly3 as well as DLBCL cells lines including SU-DHL-4, WSU-DLCL-2, TMD8 and U2932 were cultured in Roswell Park Memorial Institute (RPMI, #SH30809.01; Hyclone, Logan, UT, USA). KG-1 and MV-4-11 cells were cultured in Iscove's Modified Dulbecco's Medium (IMDM, #SH30228.01; Hyclone). All these cell lines were purchased from the American Type Culture Collection (ATCC, Manassas, VA, USA), cultured in medium containing 10% fetal bovine serum (FBS, #16000-044, Gibco), 100 U/mL penicillin, and 100 μg/mL streptomycin (#15140122, Thermo Fisher Scientific, MA, USA) at 37 °C under 5% CO_2.

For the generation of HEK293T cell lines stably expressing IKZF1-HiBiT, IKZF2-HiBiT, IKZF3-HiBiT, CK1α-HiBiT, respectively, lentivirus was produced in HEK293T cells by transfection of pCSII-CMV-neosubstrate-HiBiT-IRES2-Bsd expression vector together with pCMV-VSV-G-RSV-Rev and pCAG-HIVgp vector as described in previous study [24]. HEK293T cells supplemented with 10 μg/mL polybrene (#TR-1003, Sigma-Aldrich, MA, USA) were infected with the lentivirus. After 48 h infection, puromycin (3 μg/mL) was utilized to select stable cell lines and pooled clones were screened by immunoblot analysis.

Antibodies

The following primary antibodies were used: CRBN (#71810, 1:1000), IKZF1 (#14859, 1:1000), IKZF2 (#42427, 1:1000), IKZF3 (#15103, 1:500) and were all from Cell Signaling Technology, Boston, MA, USA; CK1α (#ab108296, 1:1000) and ZNFX1 (#ab179452, 1:500) were purchased from Abcam, MA, USA; BRD9 (#24785-1-AP, 1:1000), GSPT1 (#10763-1-AP, 1:1000), STAT5 (#13179-1-AP, 1:500), c-Myc (#10828-1-AP, 1:1000), MDM2 (#27883-1-AP, 1:1000), P53 (#1044-1-AP, 1:1000), P21 (#10355-1-AP, 1:500), DTWD1 (#26810-1-AP, 1:1000), MBD3 (#14258-1-AP, 1:1000), MNT (#23742-1-AP,

1:1000) and MBD1 (#29998-1-AP, 1:1000) were purchased from Proteintech, Rosemont, IL, USA; ZMIZ2 (#GTX118779, 1:1000) were purchased from GeneTex, San Antonio, TX, USA; ZFP91 (#CSB-PA504466, 1:1000) was purchased from Cusibio, Houston, TX, USA; Anti-rabbit IgG (HRP-conjugated, Cell Signaling Technology, #7074, 1:5000), anti-mouse IgG (HRP-conjugated, Cell Signaling Technology, #7076, 1:5000) were used as secondary antibodies.

NCI-H929 CRBN knock-out

$CRBN^{-/-}$ NCI-H929 cells were created using CRISPR-Cas9 technology. NCI-H929 cells (1×10^6 cells/well) were cultured in 6-well dishes and were transiently transfected with Plasmid Transfection Medium (#sc-108062) pre-complexed of CRBN CRISPR/Cas9 KO plasmid (#sc-412142), CRBN HDR plasmid (#sc-412142-HDR), and UltraCruz® Transfection Reagent (#sc-395739) following the instructions provided by the manufacturer (Santa Cruz Biotechnology, Inc, Dallas, TX, USA). After 72 h infection, puromycin (3 μg/mL) was utilized to select stable cell lines. Transfected cells (GFP^+) were single-cell sorted by flow cytometry into 96-well tissue culture-treated plates 7 days, and isolated single cell clones were screened by DNA sequencing and western blot analysis.

Clinical specimens, cell culture and correlation analysis

The use of human experimental materials related to this study, including cDNA derived from cell lines and clinical specimens (the clinical specimens used in this study were mainly various specimens of multiple myeloma). The patients' inclusion diagnosis and exclusion criteria; the information of clinical specimens; collection and preparation of clinical specimens were descripted in our previous publication [25] according to the NCCN Clinical Practice Guidelines in Oncology (NCCN Guidelines®), based on the Durie and Salmon, ISS and R-ISS prognostic staging criteria.

Briefly, the Diagnosis, inclusion and exclusion criteria of patients with multiple myeloma: (1) for patients with bone tumor or extra-bone tumor, biopsy-proven solitary lesion of bone or soft tissue results consisting clonal plasma cells; normal-random bone marrow biopsy results with no evidence of clonal plasma cells; normal skeletal survey, MRI or CT results except for the primary solitary lesion; absence of end-organ damage. (2) for patients with intraosseous / intra-marrow MM (e.g. the plasma cell myeloma), percentage ≥ 10% of clonal bone marrow plasma cell or biopsy-proven plasmacytoma ≥ 1 of the following myeloma-defining events. (3) patients with blood / intra-blood MM (e.g. the plasma cell leukemia), at circulating plasma cells for least 20% and in peripheral blood of at least 2×10^9/L a total plasma cell count.

In this study, clinical specimens were used for two purposes: (1) the cDNA samples reversely transcripted by total RNA from clinical specimens descripted in our previous publication [25]; (2) Patient-derived cell lines prepared from clinical specimens. The clinical specimens including (1) 35 samples of intra-marrow MM; (2) 42 samples of intra-blood MM; (3) 38 samples of MM with bone-tumor tissues in the form of masses or lumps; and (4) 21 MM samples with long-distance metastasis, or extra-bone masses or lumps forming a solid tumor tissue or mass in other organs.

The protocol of preparation PDCs was descripted in our previous publication [25]. Briefly, for the MM cells in the bone, the bone marrow aspirate was directly sorting by CD38 ($CD38^+$); (2) for the cells in peripheral blood, the peripheral blood lymphocytes are directly sorting by $CD38^+$; (3) for cells in bone tumors, the tumor tissue was abraded by using a pre-sterilized 200-mesh steel sieve by the DMEM with 20% FBS to single-cell suspension and the single-cell suspension was washed; (4) for cells in peripheral organ tumors, the tumor tissue was abraded by using a pre-sterilized 200-mesh steel sieve by the DMEM with 20% FBS to single-cell suspension and the single-cell suspension was washed. The PDC lines were generated for one cell line by one patient only. PDC-1 (patients derived cell No. 1) and PDC-3 were directly separated, cultured, and stored (PDC-1 generated from intra-marrow MM patient; PDC-3 was generated from intra-blood MM patient). PDC-5 was generated from bone-tumor tissues, and PDC-7 was generated from extra-bone tumor tissues. As control, the primary B cells which not only derived from patients with multiple myeloma which were derived from PBMC from patients; but primary B cells from healthy individuals which were derived from the peripheral blood lymphocytes of the remaining part of the whole peripheral blood provided by the blood transfusion department except plasma and red blood cells. The primary B cells were purified based on the $CD19^+/CD45^+/CD38^-$sorting. In the cell sorting process, the purity of primary B cells isolated from healthy human PBMCs could reach 99%; the purity of primary B cells isolated from patients could also reach 95–99%. When patient-derived cell lines were isolated from multiple myeloma patients, the purity of the cell lines isolated from peripheral blood was over 95% (up to 98-99%), and the purity of patient-derived cell lines isolated from tumor tissue was over 90%.

The correlation between the expression of BRD9 with IKZF1, IKZF2, IKZF3 and CK1α, respectively, were detected. At this time, taking the expression level of BRD9 as the abscissa and the expression of CRBN as the ordinate, each specimen can correspond to a data point. A group of specimens can correspond to a group of data

points, which can be fitted and linearly regressed to obtain a regression equation and P value.

Cell viability and drug synergy assays

In order to screen the molecular glue library in MM, AML and DLBCL cell lines, RPMI-8226, NCI-H929, MV4-11, U937, and WSU-DLCL-2 cells were cultured in the complete medium recommended by the vendor. The cells were seeded in corning BC white 96-well assay plates at a density of 12,000 cells per well. During the experimental period of 4 days, the cells were treated with DMSO, thalidomide, lenalidomide, pomalidomide, CC-122, or the corresponding compounds at specific concentrations as indicated.

To assess the inhibitory effect of synthesized degraders, MM, AML and DLBCL cells were cultured in 96-well plates with DMSO, pomalidomide, or the corresponding compounds at specified concentrations for a duration of 4 days. The compounds' ability to inhibit cell proliferation was evaluated using a cell counting kit-8 (CCK-8 Kit) following the instructions provided by the manufacturer (Dojindo Laboratories, Mamoto Ken, Japan).

Drug synergy assays were conducted by seeding cells in 96-well plates (100 µL per well) at a density of 12,000 cells per well. The cells were then treated with the specified drug doses for a duration of 96 h, with DMSO serving as the control. Cell viability was assessed using the CCK-8 Kit, following the manufacturer's instructions. The synergy score plots for the indicated drug combinations were calculated using SynergyFinder.

Protein preparation and molecular docking

The crystal structure of CRBN with lenalidomide was downloaded from Protein Data Bank (PDB) entry 4TZ4 [26]. The proteins were prepared using Maestro by Protein Preparation Wizard, and the missing side chains and loops were filled by Prime [27]. The ionization state of the ligand suitable for pH 7.0±2.0 was predicted by Epik [28] with the OPLS3 force field [29]. Grids for the binding site were defined using the crystal structure through Receptor Grid Generation. Ligands were docked into CRBN by Glide SP with default parameters.

MD simulations and binding free energy calculation

The CRBN underwent 500 ns MD simulation using Gromacs 2021.7 [30]. The lenalidomide and other ligands were parameterized with the general AMBER force field (GAFF) [31], and their topology and parameter files were prepared using the antechamber module [32], further converted into the GROMACS format using ACPYPE [33]. The simulation system was filled with TIP3P water to solvate the protein-ligand complexes. The AMBER14sb force field [34] was used throughout the calculation steps, followed by the addition of Na^+ and Cl^- in the water to render the system neutralized. And the sodium chloride molecules were added to reach the physiological concentration of 0.15 M. To eliminate unfavorable contacts between the protein and water molecules in the system, energy minimization and pre-equilibration simulations were conducted in three sections before the production simulation. The system was minimized by 5000 steps or Fmax < 10, and the 100 ps NVT and 1.0 ns NPT pre-equilibration was performed with time steps of 2 fs. The Particle-Mesh-Ewald (PME) method was used to calculate long-range electrostatic interactions, with the reference temperature of 310 K. H-bonds were constrained with the LINCS algorithm [35], and the Van der Waals cutoff was 1.0 nm. For pre-equilibration, the Nose-Hoover and Berendsen methods were employed for temperature and pressure coupling respectively. Finally, the production MD simulation was conducted at NPT ensemble with Nose-Hoover temperature coupling and Parrinello-Rahman pressure coupling after the system had been well-equilibrated at the desired temperature and pressure. The binding free energy of degraders were calculated using Molecular Mechanics/Poisson Boltzmann Surface Area (MM/PBSA) method.

Cell apoptosis assay

Cells (1×10^6 cells/well) were cultured in 6-well dishes. Subsequently, the cells were treated with a medium containing different concentrations of compounds for 3 days. To analyze cell apoptosis, the apoptosis rates were measured using the Annexin V-FITC apoptosis detection kit (Abcam, MA, USA). Sample analysis was performed using a FACS Calibur Flow Cytometer (Becton Dickinson, Franklin Lakes, NJ, USA).

Quantitative degradation assay using HiBiT system

To assess protein degradation of IKZF1, IKZF2, IKZF3, and CK1α, HEK293T cells that were stably expressing IKZF1-HiBiT, IKZF2-HiBiT, IKZF3-HiBiT, or CK1α-HiBiT were cultured in 96-well plates at a density of 12,000 cells per well. These cells were then treated with either DMSO or molecular glue degraders for a duration of 24 h. Subsequently, the cells were lysed using the Nano-Glo HiBiT Lytic Detection System (N3040, Promega) as per the manufacturer's instructions. The luminescent signals of the HiBiT-tagged neosubstrates were detected using the SpectraMax iD3 (Molecular Devices) instrument.

Immunoblot analysis

Cells were seeded in 6-well plates and treated with various concentrations of compounds for the specified durations. Afterwards, the cells were washed with phosphate-buffered saline (PBS) and lysed using RIPA buffer. The protein concentration was measured, and the total

protein lysates were then subjected to separation by 10% SDS-PAGE and transfer onto a nitrocellulose membrane. The membranes were subsequently probed with specific primary and secondary antibodies, and imaging was performed using the Bio-Rad Imaging system (Hercules, CA, USA).

RT-qPCR

RNA samples of MM patient cells or hematological cancer cells were isolated and extracted using TRIzol reagent according to the manufacturer's instructions (Invitrogen). A minimum of 2 μg of total RNA was reverse transcribed into first strand cDNA with oligo (dT) primers using Moloney murine leukemia virus reverse transcriptase (Promega, Madison, WI USA). Quantitative polymerase chain reaction (qPCR) was performed in triplicates in a 20 μL reaction mixture containing 10 μL of SYBR Premix Ex Taq Master Mix (2×) (Takara Bio, Shiga, Japan), 0.5 mM of each of the primers and 10 ng cDNA. The relative expression level of the target was calculated using the comparative Ct method. β-actin was used as an internal control to normalize sample differences. The primers used in qPCR experiments were available in Table S1.

MS-based proteomic analysis

Sample preparation NCI-H929 cells were treated with DMSO or **MGD-4** (1, 10 μM), **MGD-28** (1, 10 μM), pomalidomide (10 μM) and CC-220 (1 μM) for 4 h. Afterward, the cells were washed with PBS three times and lysed using 8 M UA (8 M urea, 100mM Tris-HCl, pH 8.0) containing complete protease inhibitor tablets. The supernatant was then collected by centrifuging the lysed cells at 14,000 rpm for 15 min at 4 °C. The collected supernatant was reduced with 10 mM Tris (2-carboxyethyl) phosphine hydrochloride solution (TCEP) at room temperature for 30 min, followed by cysteine alkylation with 50 mM 2-chloroacetamide (CAA) at room temperature for 30 min. Subsequently, the denatured proteins were digested overnight at 37 °C using trypsin (at a 1:50 ratio of enzyme to protein). The reactions were quenched by adding formic acid (FA) to a final concentration of 0.1%. To identify substrates targeted by **MGD-4**, **MGD-28**, or other IMiDs, samples were desalted and subjected to label-free proteomics analysis. For the investigation of substrates involved in IMiDs resistance mechanisms, samples were desalted, then labeled with TMTpro^{TM}-16plex reagents, and subsequently combined and desalted again for mass spectrometry analysis. TMT labeling steps were performed according to the manufacturer's instructions, and the labeling channel design was described as followed: 126 QC; 127 N, 127 C, 128 N, 128 C, and 129 N represented five biological replicates of wild-type cells; 129 C, 130 N, 130 C, 131 N, and 131 C represented five biological replicates of cells resistant to lenalidomide; 132 N, 132 C, 133 N, 133 C, and 134 N represented five biological replicates of cells resistant to pomalidomide.

LC–MS/MS analysis For samples to identify the substrates of **MGD-4**, **MGD-28**, and other IMiDs, the corresponding peptide mixtures were analyzed using an EASY-nLC 1200 liquid chromatography system (Thermo Fisher Scientific) with a home-made 15 cm C18 column (ID 150 μm, 1.9 μm, 100 Å). Peptide separation was carried out over a 78-minute gradient at a constant flow rate of 600nL/min: 7–12% B in 8 min, 12–32% B in 45 min, 32–45% B in 13 min, 45–95% B in 2 min, followed by a 10-minute hold at 95% B (Buffer A: 0.1% FA, Buffer B: 0.1% FA in 80% acetonitrile), with an additional 15-minute wash. The peptide mixture was analyzed using an Orbitrap Fusion mass spectrometer (Thermo Fisher Scientific). MS data were acquired using a data-dependent acquisition (DDA) method, with a dynamic exclusion duration of 18 s. For the MS1 scan, mass spectra were acquired in the positive-ion mode in the range of 300–1400 m/z, with a maximum ion injection time of 50ms and a resolution of 120,000 at m/z 200. Fragmentation of precursor ions was achieved by higher-energy collision dissociation (HCD) with a normalized collision energy of 33%. The MS2 spectra were acquired with an automatic gain control target value of 1.0e4 and a maximum injection time of 35 ms.

For samples to investigate the resistance mechanisms of lenalidomide and pomalidomide, the corresponding samples were analyzed using Orbitrap Exploris 480 mass spectrometer coupled with a high-field asymmetric waveform ion mobility spectrometer using −45 V and −65 V. The peptides were trapped in a home-made 2 cm solid-phase extraction column (ID 100 μm) and separated by a home-made 20 cm C18 column (ID 75 μm, 1.9 μm, 100 Å) with a constant flow rate of 300nL/min. The gradient was 7–12% B in 10 min, 12–30% B in 80 min, 30–45% B in 20 min, 45–95% B in 1 min, followed by a 9-minute hold at 95% B (Buffer A: 0.1% FA, Buffer B: 0.1% FA in 80% ACN), with an additional 15-minute wash. MS data were acquired using a data-dependent acquisition (DDA) method, with a dynamic exclusion duration of 30 s. MS1 scan was conducted at mass range of 375–1400 m/z, with a maximum ion injection time of 50 ms and a resolution of 120,000 at m/z 200. HCD energy was 34%. The MS2 spectra were acquired with resolution of 45,000, isolation window of 0.5 m/z, and maximum injection time of 120 ms.

MS data analysis The label-free MS raw files were analyzed using MaxQuant (version 2.0.3.0), while the TMT-labeled MS files were analyzed using Proteome Discoverer (PD) (version 2.5.0.400). Both were matched against the UniProt Human database (downloaded in Sep 2022, con-

taining 20398 entries). The protease was set as trypsin/P with a maximum of two missed cleavages. Carbamidomethyl (C) was designated as a fixed modification, while Oxidation (M) and Acetyl (Protein N-term) were defined as variable modifications. A false discovery rate (FDR) of ≤0.01 was applied at the spectra, protein, and modification levels. All other settings remained as default. Proteins identified from the contaminated and reversed database were excluded. The protein groups results generated by MaxQuant and PD were subsequently analyzed in R (version 4.2.1). Statistical analysis was performed using student's t-test, and p values < 0.01 were considered statistically significant.

Data availability All the mass spectrometry proteomics data have been deposited to the ProteomeXchange Consortium (https://proteomecentral.proteomexchange.org) via the iProX partner repository [36, 37] with the dataset identifier PXD053334.

Animal models for tumor growth

Animal research was conducted in accordance with the guidelines of the Animal Care and Use Committee of the Beijing Institute of Biotechnology. Six-week-old BALB/c nude mice and Non-obese diabetic Severe combined immunodeficiency (NOD/SCID) mice were obtained from SiPeiFu company, Beijing, China, and housed in a specific pathogen-free (SPF) animal facility. NCI-H929 cells (5×10^6) were injected subcutaneously into the dorsal flank of mice. For the evaluation of our compounds as single agent, once the NCI-H929 tumor volume reached approximately 80 mm^3, BALB/c nude mice were divided into six groups and were treated with pomalidomide (10 mg/kg, *p.o.*/qd), **MGD-4** (3, 10 mg/kg, p.o./qd), **MGD-28** (3, 10 mg/kg, *p.o.*/qd), and a vehicle control (10% DMSO+10% PEG300+5% Tween 80+75% H_2O, *p.o.*/qd) for 18 days. For the drug synergy assays, once the NCI-H929 tumor volume reached approximately 80 mm^3, the BALB/c nude mice were divided into six groups and treated with single-agent dexamethasone (3 mg/kg, *p.o.*/qd), **MGD-4** (3 mg/kg, *p.o.*qd), **MGD-28** (3 mg/kg, *p.o.*/qd), and a vehicle control (10% DMSO+10% PEG300+5% Tween 80+75% H_2O, *p.o.*/qd), as well as combination treatments of dexamethasone+**MGD-4** and dexamethasone+**MGD-28** for 14 days. To evaluate the synergistic effect of **MGD-28** with bortezomib/tazemetostat, once the NCI-H929 tumor volume reached approximately 80 mm^3, the NOD/SCID mice were divided into six groups and treated with single-agent **MGD-28** (3 mg/kg, *p.o.*/qd), bortezomib (1 mg/kg, *p.o.*/qd), tazemetostat (100 mg/kg, *p.o.*/qd), and a vehicle control (10% DMSO+10% PEG300+5% Tween 80+75% H_2O, *p.o.*/qd), as well as combination treatments of **MGD-28**+bortezomib and **MGD-28**+tazemetostat for 12 days. To evaluate the synergistic effect of I-BRD9 with **MGD-28**/pomalidomide, once the NCI-H929 tumor volume reached approximately 80 mm^3, the NOD/SCID mice were divided into six groups and treated with single-agent pomalidomide (10 mg/kg, *p.o.*/qd), **MGD-28** (3 mg/kg, *p.o.*/qd), I-BRD9 (10 mg/kg, *p.o.*/qd), and a vehicle control (10% DMSO+10% PEG300+5% Tween 80+75% H_2O, *p.o.*/qd), as well as combination treatments of I-BRD9+**MGD-28** and I-BRD9+pomalidomide for 24 days. The tumor volume was calculated using the formula V = (longest diameter × shortest diameter^2)/2. Tumor growth inhibition (TGI) was calculated to determine the inhibitory strength of the drugs on tumor growth. TGI (%) = $(V_c - V_t) / (V_c - V_0) \times 100$, where V_c is the median volume of the control group, V_t is the median volume of the treated groups at the end of the study, and V_0 is the median volume of the control group at the start of the study. The body weight of the mice was measured every 2 days. The experiment was terminated when the maximum tumor size reached approximately 1.5 cm in diameter. Euthanasia was performed under deep anesthesia, and the tumors were then isolated from the animals, weighed, and photographed.

Pharmacokinetic experiments in rats

Pharmacokinetic experiments in rats Animal experiments were conducted at the Beijing Center for Drug Safety Evaluation, which is approved by the Institutional Animal Care and Use Committee of the Center. These experiments were conducted in accordance with the guidelines set forth by the Association for Assessment and Accreditation of Laboratory Animal Care International (AAALAC). Male Sprague-Dawley (SD) rats weighing between 180 and 210 g were obtained from Beijing Vital River Laboratory Animal Technology Co., Ltd. and were kept in a controlled environment with regulated temperature, humidity, and a 12-hour light/dark cycle. It was determined that live animals were necessary to achieve the study objectives, as no alternative methods were available. The compounds **MGD-4** and **MGD-28** were dissolved in a 5% glucose solution, with a final concentration of less than 2% DMSO. A total of 24 rats were randomly divided into four groups and administered **MGD-4** and **MGD-28** via intravenous bolus (1 mg/kg) and gavage (3 mg/kg), respectively. Rats in the oral administration group underwent a 12-hour fasting period before drug administration, with unrestricted access to water. Blood samples (0.15 mL) were continuously collected prior to administration and at designed time points up to 24 h post intravenous dosing, and oral administration. These blood samples were collected in heparin anticoagulation collection tubes, centrifuged at 4℃ for 10 min (2500 × g) to separate the plasma, and then stored at -20℃. Prior to determining the plasma drug concentration, the samples

were thawed at room temperature and a 20 μL plasma sample was taken for quantitative extraction. Acetonitrile (20 μL) and IS (propranolol 10 ng/mL, 100 μL) were added to precipitate the protein through vortexing. After centrifugation at 15,000 g for 10 min, the supernatant was collected and a 5 μL aliquot of the sample was injected into the LC-MS/MS system for drug concentration determination.

Bioanalysis method The concentrations of **MGD-4** and **MGD-28** were determined using an LC-MS/MS system. The system consisted of an LC instrument (LC-20AD, Shimadzu) and an 8060 triple quadrupole mass spectrometer detector (Shimadzu, Japan). The compounds were separated on a Phenomenex C18 column (2.1×50 mm, USA). An LC gradient was employed, which consisted of a 0.1% formic acid aqueous solution (v/v, mobile phase A) and a 0.1% formic acid in acetonitrile (v/v, mobile phase B). The flow rate was set at 0.6 mL/min, and the run duration was 4 min. The LC separation program was set as follows: 0–0.3 min, 5% B; 0.3–2.0 min, a gradient from 5 to 95% B; 2.0–2.5 min, held at 95% B; 2.6 min, returned to 5% B. The analytes and internal standard were detected using positive ion spray in the multiple-reaction-monitoring modes (MRM). The injection volume was 5 μL. The monitored precursor/product ion mass transitions were as follows: m/z 289.05/178.1 for **MGD-4**, m/z 596.2/307.95 for **MGD-28**, and m/z 260.1/116.1 for propranolol (IS). The calibration linear ranges for both **MGD-4** and **MGD-28** were 1-1000 ng/mL.

Data analysis The pharmacokinetic parameters were calculated using WinNonlin 9.0 (Pharsight, CA) by noncompartmental method. The maximal plasma concentration (C_{max}) and time to reach the peak (T_{max}) were obtained directly from the observed data. The area under the plasma concentration-time curve (AUC) from time 0 to the last time point with a measurable concentration was calculated using the trapezoidal method. The area from the last datum point to time infinity was estimated by dividing the last measured plasma concentration by the terminal rate constant. The terminal elimination rate constant (λ_z) was calculated by log-linear regression of the terminal phase of the plasma concentration-time curves using at least three time points, and the half-life $t_{1/2}$ was calculated from $\ln 2/\lambda_z$. Absolute bioavailability was evaluated calculated as: bioavailability (F, %) = $[(AUC_{extra-venous\ route} / AUC_{iv}) \times dose_{iv}/dose_{extra-venous\ route})] \times 100$.

Statistical analysis was conducted by Student's *t* test between different groups for major pharmacokinetic parameters (C_{max}, T_{max}, AUC, volume of distribution (V), and clearance (CL). A P-value < 0.05 was considered statistically significant.

Statistical analysis and reproducibility

All in vitro experiments were conducted in triplicate. Differences between variables were evaluated using the Bonferroni correction, two-tailed Student's t-test or one-way analysis of variance (ANOVA). Statistical analyses were performed using SPSS 13.0 or GraphPad Prism 8.0. The statistical data were expressed as the mean ± standard deviation (SD). A P value < 0.05 was considered statistically significant for all assays.

Results

Phenotypic screening of a compound library against multiple hematological cancer cell lines

Use of cell-based phenotypic screening of a small molecule compound library in multiple cell lines allows for triaging and prioritization of hits based on their specificity to cell lines. We performed library screening to detect the inhibition of cell viability in five hematological cancer cell lines (RPMI-8226, NCI-H929, MV-4-11, U937, and WSU-DLCL-2). This procedure was performed to encompass a wider range of genetic diversity and vulnerabilities related to cancer. As depicted in Fig. 1A and B, compounds were clustered based on their activity profiles across the cancer cell line panel. Notably, the prototypical IMiDs (thalidomide, lenalidomide, and pomalidomide) displayed limited potency, with half-maximal inhibition concentrations (IC_{50}) values in the micromolar range (red box). CC-122 demonstrated potent cytotoxicity against NCI-H929 cell lines, with an IC_{50} value below 0.33 μM (blue box). Several hits with a novel phthalazinone skeleton exhibited activity in NCI-H929 and MV-4-11 cells, with IC_{50} values below 1 μM (Fig. S1A). Among the identified hits, compound **MGD-4** exhibited the most pronounced antiproliferative activity, particularly in NCI-H929 and MV-4-11 cells, with IC_{50} values below 0.33 μM. The antiproliferative efficacy of **MGD-4** was next evaluated in a panel of MM, AML, and DLBCL cell lines. As illustrated in Fig. 1C, **MGD-4** displayed potent inhibitory activity, with IC_{50} values ranging from submicromolar to single-digit micromolar concentrations in MM and AML cell lines. These values were comparable to those of CC-122 and significantly higher than those of thalidomide, lenalidomide, and pomalidomide, particularly in AML cell lines. In DLBCL cell lines, the compounds exhibited moderate IC_{50} values, with concentrations ranging from single-digit to double-digit micromolar values. This result indicated a low level of cytotoxicity against the DLBCL cell lines (Fig. S1 B). The ability of **MGD-4** to induce cell apoptosis was investigated in subsequent. The apoptosis rates resulting from **MGD-4** treatment at 10 μM in NCI-H929 and MV-4-11 cells were 52.1% and 41.0%, respectively. These rates were significantly higher than those produced by pomalidomide treatment at 10 μM (35.1% and 14.8% respectively)

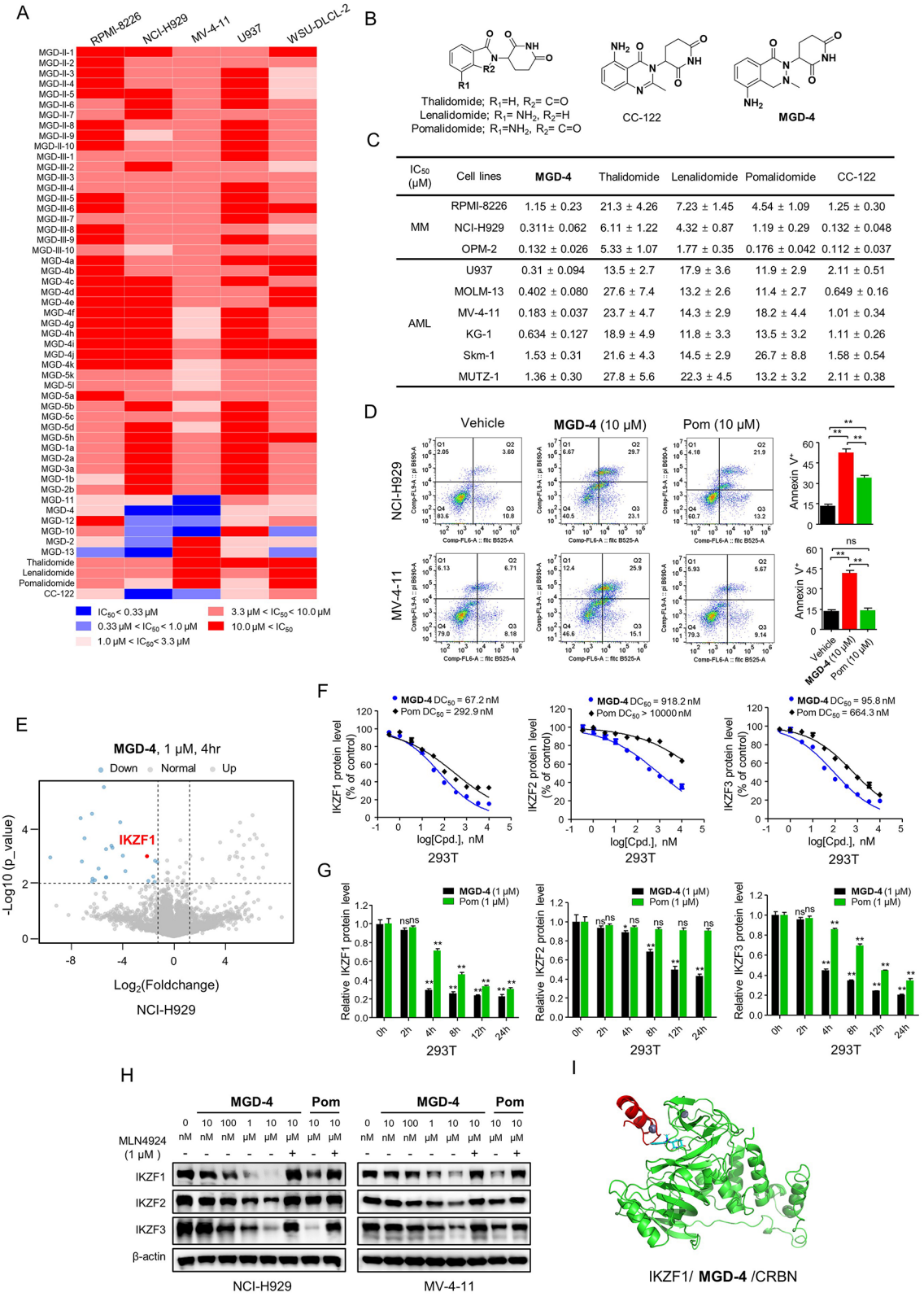

Fig. 1 (See legend on next page.)

(See figure on previous page.)

Fig. 1 Phenotypic screening of a compound library against multiple hematological cancer cell lines. **A**. Heat map of 49 compounds with IMiDs controls (thalidomide, lenalidomide, pomalidomide and CC-122) screened against five different cell lines (RPMI-8226, NCI-H929, MV-4-11, U937, and WSU-DLCL-2) for antiproliferative effects. Viability assay performed in cancer cells treated with indicated compound for 96 h to obtain IC_{50} values. Means of three independent experiments are shown. **B**. Chemical structures of thalidomide, lenalidomide, pomalidomide, CC-122 and **MGD-4**. **C**. IC_{50} values of **MGD-4**, thalidomide, lenalidomide, pomalidomide and CC-122 in MM and AML cell lines for 96 h. Mean ± SEM of three independent experiments is shown. **D**. Flow cytometry plot showing NCI-H929 and MV-4-11 cells treated with vehicle, **MGD-4** (10 μM) or pomalidomide (Pom, 10 μM) for 3 days and cells were stained with Annexin V-PE and DAPI. Histograms show the relative cell percentage of apoptosis in NCI-H929 and MV-4-11 cells. Error bars denote standard deviations (independent experiments, $n = 3$), ns (no significance), $^{**}p < 0.01$ (one-way ANOVA). **E**. Proteomics analysis of NCI-H929 cells treated for 4 h with **MGD-4** (1 μM). **F**. Levels of IKZF1 (left), IKZF2 (middle) and IKZF3 (right) in engineered HEK293T (293T) cells with increasing doses of **MGD-4** for 24 h as determined by IKZF1-, IKZF2- and IKZF3-HiBiT assay, respectively. Data shown are a representative graph of three independent experiments; mean ± SD of triplicates. **G**. Levels of IKZF1 (left), IKZF2 (middle) and IKZF3 (right) in engineered 293T cells with increasing treatment time of **MGD-4** (0.1 and 1.0 μM) or pomalidomide (Pom, 0.1 and 1.0 μM) as determined by IKZF1-, IKZF2- and IKZF3-HiBiT assay, respectively. Error bars denote standard deviations (independent experiments, $n = 3$). Student's t test, ns (no significance), $^{*}p < 0.05$, $^{**}p < 0.01$. **H**. Western blot analysis of Ikaros family members in NCI-H929 and MV-4-11 cells treated with the indicated compound for 24 h with or without MLN4924 1 h pretreatment. **I**. The docking models of **MGD-4** to the IKZF1-CRBN

(Fig. 1D). In accordance with its moderate antiproliferative efficacy in WSU-DCLC-2, the apoptosis rate following treatment with **MGD-4** at 10 μM was 16.5%, whereas pomalidomide at 10 μM demonstrated no efficacy (Fig. S1C).

To investigate the targets of **MGD-4** in an unbiased manner, we performed quantitative proteomics in NCI-H929 cells treated with 1 μM **MGD-4** for 4 h. IKZF1 protein was significantly downregulated following **MGD-4** treatment (Fig. 1E), suggesting that **MGD-4** recruits transcription factors related to Ikaros family and promotes their ubiquitination and proteasomal degradation. To quantitatively analyze the ability and kinetics of **MGD-4** for Ikaros family neosubstrate degradation, we generated HEK293T cells stably expressing neosubstrate-HiBit using a lentivirus and investigated the degradation depth, kinetics, and potency of these hit compounds. The luminescence signals of IKZF1-, IKZF2-, and IKZF3-HiBit were markedly reduced after treatment at concentrations of 0.1 and 1 μM for 24 h, with **MGD-4** exhibiting the most robust protein degradation efficacy (Fig. S1D-S1F). Treatment with **MGD-4** led to a dose-dependent degradation of IKZF1 (half-maximal degradation concentration [DC_{50}] = 67.2 nM, maximal degradation [D_{max}] = 84.9%), IKZF2 (DC_{50} = 918.2 nM, D_{max} = 64.6%), and IKZF3 (DC_{50} = 95.8 nM, D_{max} = 81.2%). **MGD-4** exhibited a more potent degradation effect than pomalidomide on IKZF1 (DC_{50} = 292.9 nM, D_{max} = 75.1%), IKZF2 (DC_{50} > 10,000 nM), and IKZF3 (DC_{50} = 664.3 nM, D_{max} = 64.1%) (Fig. 1F). Furthermore, time-dependent experiments demonstrated that pomalidomide treatment at 1 μM weakly reduced IKZF1and IKZF3 after 4 h of treatment, with reductions of less than 30% and less than 20%, respectively. In contrast, pomalidomide treatment had no effect for IKZF2. However, **MGD-4** demonstrated a substantial reduction in IKZF1 (>70%) and IKZF3 (>50%) after 4 h of treatment, and a reduction in IKZF2 (>50%) after 12 h of treatment (Fig. 1G). Similarly, **MGD-4** exhibited higher endogenous IKZF1, IKZF2 and IKZF3 degradation potency over pomalidomide at micromolar concentrations in a Cullin-dependent manner, as evidenced by western blotting (Fig. 1H). To gain insight into the molecular basis of **MGD-4**-directed substrate recruitment to CRBN, we analyzed the docking poses at the IMiD-binding sites of the IKZF1-CRBN complex. In our docking simulation using Schrödinger software, lenalidomide and pomalidomide bound to the IKZF1-CRBN complex in a manner consistent with the previously determined structures (Fig. S1G, S1H). Our findings indicate that **MGD-4** exhibited nearly identical binding modes to those observed for lenalidomide and pomalidomide. This result was evidenced by the glutarimide ring of **MGD-4** being exposed on the surface of CRBN, whereas the phthalazinone ring of **MGD-4** was oriented toward the β-hairpin structure of IKZF1 (Fig. 1I). Because lower binding energy (ΔG) indicates more potent bond affinity and a more stable protein complex, the ΔG values of the synthesized compounds were also determined. **MGD-4**-recruited CRBN complex exhibited a lower ΔG values of -87.76 kJ/mol compared with pomalidomide (-74.81 kJ/mol) and lenalidomide (-75.13 kJ/mol) (Fig. S1I), indicating the more stability of **MGD-4**-CRBN complex. These results collectively demonstrate that **MGD-4** exhibits potent antiproliferative effects in MM and AML cells through the CRBN-mediated degradation of IKZF1, IKZF2 and IKZF3, which could act as a lead compound for further optimization.

Rational optimization of CK1α degraders using molecular dynamics

Given the pivotal role of CK1α in the development of hematological cancer, we assessed the effect of **MGD-4** on CK1α degradation in HEK293T cells stably expressing CK1α-HiBit. As illustrated in Fig. S2A, lenalidomide demonstrated moderate efficacy (DC_{50} = 3.92 μM, D_{max} = 64.0%), whereas **MGD-4** and pomalidomide exhibited minimal efficacy with DC_{50} values exceeding 10 μM. We next explored the potential of multi-targeted degradation of CK1α and Ikaros proteins to enhance efficacy, using our lead compound **MGD-4**.

Lenalidomide has been clinically approved to treat MDS by inducing CRBN-mediated CK1α degradation.

The underlying molecular basis may guide the rational discovery of CK1α degraders. Comparison of the structure of lenalidomide-CRBN complex (PDB ID: 4TZ4) and crystal structure of the CRBN: lenalidomide: CK1α ternary complex (PDB ID: 5FQD) through molecular dynamics (MD) simulation showed that the conformational difference between the CRBN was manifested in inversion of the $CRBN^{Try355}$ residue. Further analysis revealed that lenalidomide induced inversion of $CRBN^{Tyr355}$ residue to enlarge the cavity of the β-hairpin structure of the CRBN. This result was reflected by the depth of the cavity, which increased from 0.44 Å to 0.81 Å, and the width of the cavity, which increased from 9.7 Å to 11.7 Å (Fig. 2A and C). These changes helped CK1α to form a stable ternary complex.

To validate this hypothesis, MD simulations of lenalidomide and CRBN were conducted for 500 ns, and the distance between Tyr355 and His357 was calculated to characterize the inversion of the Tyr355 residue. Upon inversion of Tyr355, the distance between Tyr355 and His357 may increase. As shown in Fig. 2D, MD simulation of lenalidomide with CRBN demonstrated that the Tyr355 underwent a flip, resulting in an increase in the distance between Tyr355 and His357 from approximately 0.4 to 1.15 nm during MD simulation of 400–500 ns. This process helps to form a conformation-flipped stable "CK1α-lenalidomide-CRBN" ternary complex structure (Fig. S2 A). This phenomenon was also observed in the crystal structure of the CRBN: CC-92,480 complex (PDB ID: 8D7U), in which the $CRBN^{Tyr355}$ residue was inverted (Fig. S2 B), resulting in formation of a conformation-flipped stable "CK1α-CC-92480-CRBN" ternary complex structure (Fig. S2C). In contrast, the distance between Tyr355 and His357 did not increase during MD simulations of **MGD-4** and CRBN, and the Tyr355 residue could not be inverted (Fig. 2E). These data indicate that $CRBN^{Tyr355}$ inversion plays a role in IMiDs-induced CK1α degradation.

Notably, further analysis of the binding pockets of lenalidomide for CRBN revealed that the phthalimide ring of lenalidomide is near the Tyr355 residue (Fig. 2C). We hypothesized that extension of the side chain in the 6-CH group of the phthalimide ring could help form salt bridges and hydrogen bonds with $CRBN^{Asn351}$ and $CRBN^{His353}$, and stabilize the flipped conformation of $CRBN^{Tyr355}$, enhancing the induction of CK1α degradation. Thus, we designed **MGD-15** and **MGD-18** with varying extension lengths to enable further interactions with both CRBN and CK1α (Fig. 2F). MD simulations revealed that the Tyr355 residue was flipped and the distance between Tyr355 and His357 increased (Fig. 2G and H), resulting in the formation of stable conformation-flipped "CK1α-**MGD-15**-CRBN" and "CK1α-**MGD-18**-CRBN" ternary complex structures, respectively (Fig. S3A, S3B). **MGD-15** and **MGD-18**-recruited CRBN complexes exhibited ΔG values of -101.50 and −119.56 kJ/mol, respectively (Fig. S3C), suggesting that degraders with extended the side chain promote the formation and stability of degraders-recruited CRBN complexes.

To validate this result, both compounds were synthesized and the degradation of CK1α was quantified in greater detail. **MGD-15** resulted in dose-dependent degradation of CK1α (DC_{50}=0.97 μM, D_{max} = 75.0%), and **MGD-18** exhibited even higher efficacy (DC_{50}=0.092 μM, D_{max} = 84.3%) after 24 h of treatment. These agents showed much higher potency compared with lenalidomide (DC_{50}=3.92 μM, D_{max} = 64.0%) (Fig. 2I). Similarly, for endogenous CK1α in NCI-H929 and MV-4-11 cells, **MGD-4** and pomalidomide demonstrated no efficacy in inducing CK1α degradation, whereas **MGD-15** and **MGD-18** exhibited significant efficacy in inducing CK1α degradation compared with lenalidomide (Fig. 2J and Fig. S3D). **MGD-15** and **MGD-18** also showed a more pronounced degradation capacity for IKZF1/2/3 than **MGD-4**, lenalidomide, and pomalidomide. The antiproliferative efficacy analysis of multiple hematological cancer cell lines showed that **MGD-15** displayed significantly higher inhibitory activity than **MGD-4**, and **MGD-18** demonstrated even greater inhibitory activity than **MGD-15**, with IC_{50} values ranging from double-digit nanomolar to submicromolar concentrations in MM, AML and DLBCL cell lines (Fig. 2K and Fig. S3E). These data collectively illustrate an MD-based approach for rational optimization of CK1α degraders, accompanied by significant enhancement of antiproliferative potency.

MGD-28 exhibited high antiproliferative potency and significant degradation effects on Ikaros proteins and CK1α

Building on the MD-based strategy, we further extended the side chain of **MGD-18** by adding a substituted benzene ring to obtain the degrader **MGD-28** (Fig. 3A), and subsequently investigated the effects of **MGD-28** on inversion of the $CRBN^{Tyr355}$ residue using MD simulations. The results demonstrated that **MGD-28** induced inversion of the $CRBN^{Tyr355}$ residue and enlarged the cavity of the CRBN β hairpin structure, forming a more stable ternary complex (Fig. 3B and C and Fig. S4A). Moreover, **MGD-28**-CRBN complex exhibited low ΔG values of -228.71 kJ/mol (Fig. S4B), indicating the high stability of **MGD-28**-CRBN complex. **MGD-28** induced a more robust protein degradation of CK1α-HiBit with a DC_{50} of 7.8 nM and a D_{max} of 90.1% (Fig. 3D), and treatment with 1 μM **MGD-28** for 4 h resulted in a significant reduction in CK1α by over 80% (Fig. 3E), indicating that **MGD-28** had much higher potency than lenalidomide at the same concentration and treatment time. The reduction in the luminescence signals of CK1α-HiBit was

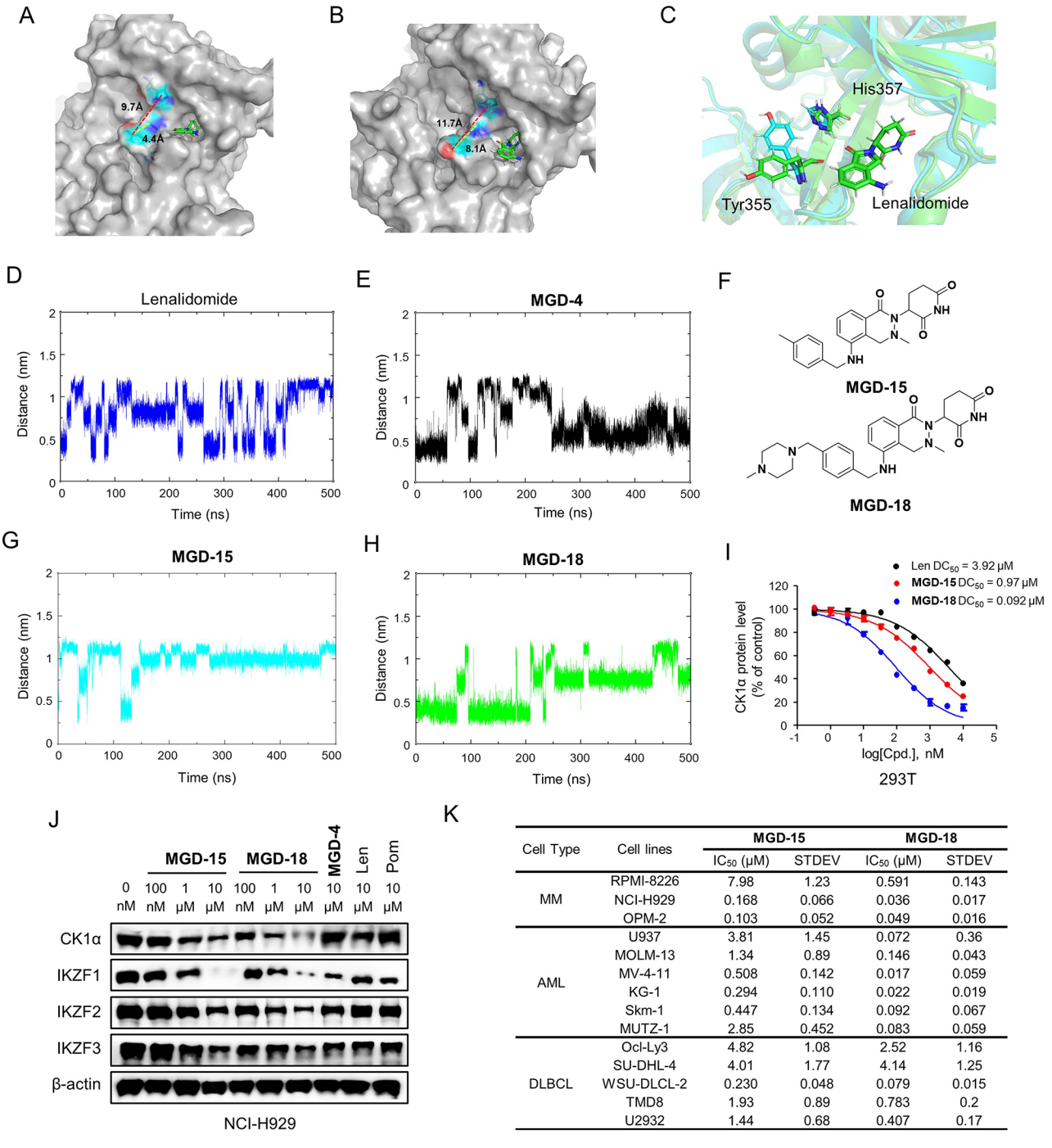

K

Cell Type	Cell lines	MGD-15		MGD-18	
		IC_{50} (μM)	STDEV	IC_{50} (μM)	STDEV
MM	RPMI-8226	7.98	1.23	0.591	0.143
	NCI-H929	0.168	0.066	0.036	0.017
	OPM-2	0.103	0.052	0.049	0.016
AML	U937	3.81	1.45	0.072	0.36
	MOLM-13	1.34	0.89	0.146	0.043
	MV-4-11	0.508	0.142	0.017	0.059
	KG-1	0.294	0.110	0.022	0.019
	Skm-1	0.447	0.134	0.092	0.067
	MUTZ-1	2.85	0.452	0.083	0.059
DLBCL	Ocl-Ly3	4.82	1.08	2.52	1.16
	SU-DHL-4	4.01	1.77	4.14	1.25
	WSU-DLCL-2	0.230	0.048	0.079	0.015
	TMD8	1.93	0.89	0.783	0.2
	U2932	1.44	0.68	0.407	0.17

Fig. 2 Rational optimization of CK1α degraders using molecular dynamics. A-B. Schematic diagram of the unflipped (**A**) and flipped (**B**) $CRBN^{Tyr355}$ residue in binding pocket induced by lenalidomide. **C.** Lenalidomide interacts with CRBN pocket amino acids. **D**-**E**. Molecular dynamics simulation of lenalidomide (**D**) and **MGD-4** (**E**) with CRBN at 500 ns. **F**. Chemical structures of **MGD-15** and **MGD-18**. **G**-**H**. Molecular dynamics simulation of **MGD-15** (**G**) and **MGD-18** (**H**) with CRBN at 500 ns. **I**. Levels of CK1α in engineered 293T cells with increasing doses of lenalidomide (Len), **MGD-15** and **MGD-18** as determined by CK1α-HiBiT assay, respectively. Data shown are a representative graph of three independent experiments; mean ± SD of triplicates. **J**. Western blot analysis of CK1αand Ikaros family members in NCI-H929 cells treated with indicated compounds for 24 h. **K**. IC_{50} values of **MGD-15** and **MGD-18** in different hematological cancer cell lines for 96 h. Mean ± SEM of three independent experiments is shown

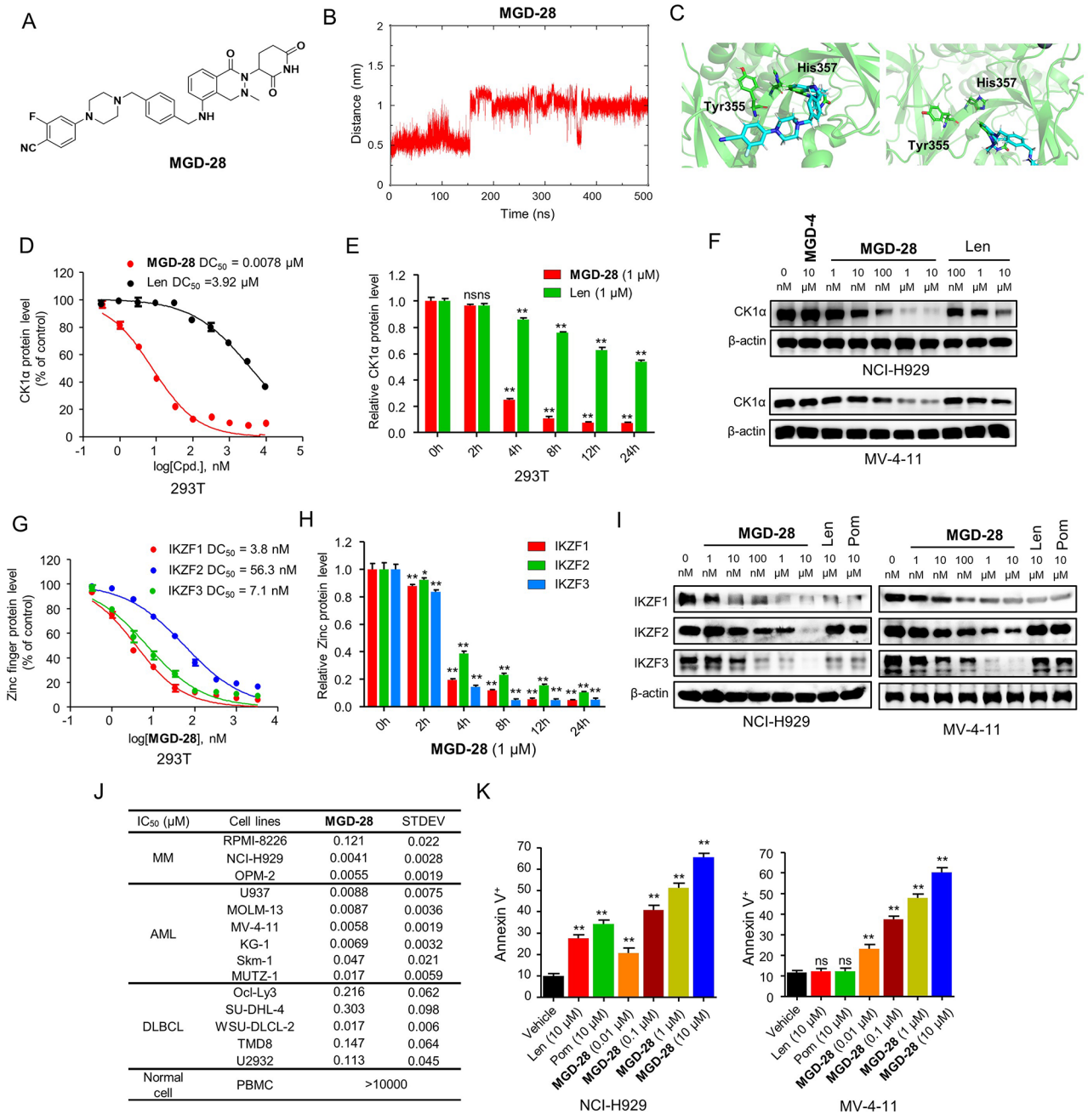

IC_{50} (μM)	Cell lines	MGD-28	STDEV
MM	RPMI-8226	0.121	0.022
	NCI-H929	0.0041	0.0028
	OPM-2	0.0055	0.0019
AML	U937	0.0088	0.0075
	MOLM-13	0.0087	0.0036
	MV-4-11	0.0058	0.0019
	KG-1	0.0069	0.0032
	Skm-1	0.047	0.021
	MUTZ-1	0.017	0.0059
DLBCL	Ocl-Ly3	0.216	0.062
	SU-DHL-4	0.303	0.098
	WSU-DLCL-2	0.017	0.006
	TMD8	0.147	0.064
	U2932	0.113	0.045
Normal cell	PBMC	>10000	

Fig. 3 **MGD-28** exhibited high antiproliferative potency and significant degradation effects on Ikaros proteins and CK1α. (**A**) Chemical structures of **MGD-28**. (**B**) Molecular dynamics simulation of **MGD-28** with CRBN at 500 ns. (**C**) Schematic diagram of $CRBN^{Tyr355}$ residue unflipped binding pocket (left) and flipping binding pocket (right) induced by **MGD-28**. (**D**) Levels of CK1α in engineered 293T cells with increasing doses of **MGD-28** or lenalidomide for 24 h as determined by CK1α-HiBiT assay, respectively. Data shown are a representative graph of three independent experiments; mean ± SD of triplicates. (**E**) Levels of CK1α in engineered 293T cells with increasing treatment time of **MGD-28** (1 μM) or lenalidomide (1 μM) as determined by CK1α-HiBiT assay, respectively. Error bars denote standard deviations (independent experiments, $n = 3$). Student's t test, ns (no significance), $^{**}p < 0.01$. (**F**) Western blot analysis of CK1α in NCI-H929 and MV-4-11 cells treated with the indicated compound for 24 h. (**G**) Levels of IKZF1 and IKZF3 in engineered 293T cells with increasing doses of **MGD-28** for 24 h as determined by IKZF1-, IKZF2- and IKZF3-HiBiT assay, respectively. Data shown are a representative graph of three independent experiments; mean ± SD of triplicates. (**H**) Levels of IKZF1, IKZF2 and IKZF3 in engineered HEK293T cells with increasing treatment time of **MGD-28** (1 μM) as determined by IKZF1-, IKZF2- and IKZF3-HiBiT assay, respectively. Error bars denote standard deviations (independent experiments, $n = 3$). Student's t test, $^{*}p < 0.05$, $^{**}p < 0.01$. (**I**) Western blot analysis of Ikaros family members in NCI-H929 cells treated with increasing doses of **MGD-28** for 24 h. (**J**) IC_{50} values of **MGD-28** in different hematological cancer cell lines and PBMC cells for 96 h. Mean ± SEM of three independent experiments is shown. **K**. Flow cytometry plot showing NCI-H929 and MV-4-11 cells treated with indicated doses of **MGD-28**, lenalidomide (Len) or pomalidomide (Pom) for 3 days, and cells were stained with Annexin V-PE and DAPI. Apoptosis was measured by flow cytometry using Annexin V as a marker. Error bars denote standard deviations (independent experiments, $n = 3$). Student's t test, ns (no significance), $^{**}p < 0.01$

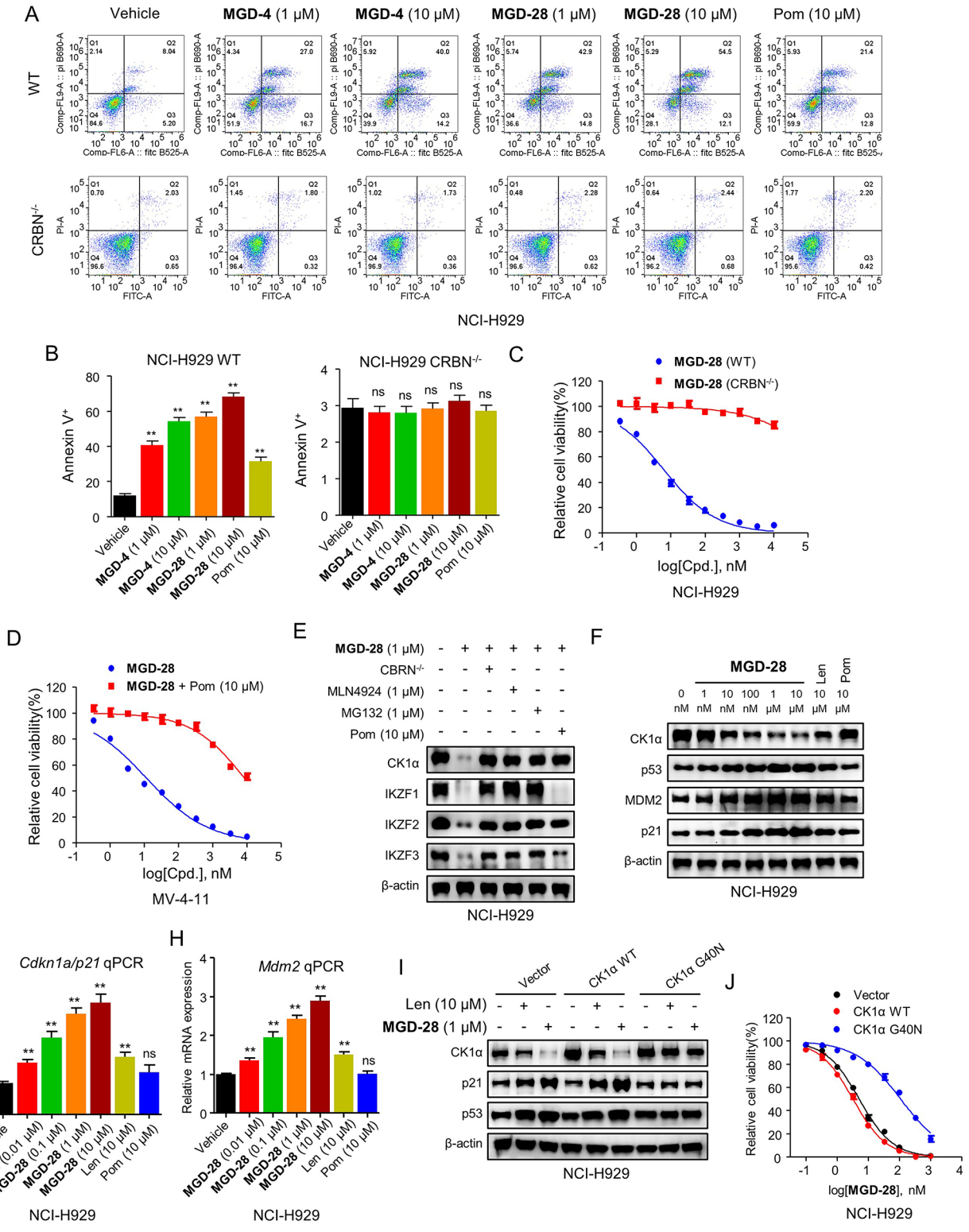

Fig. 4 (See legend on next page.)

(See figure on previous page.)

Fig. 4 **MGD-28** exhibited a significant degradation effect on IKZF1/2/3 and CK1α via a Cullin-CRBN dependent pathway. **A-B**. Flow cytometry plot showing wild type and CRBN$^{-/-}$ NCI-H929 cells treated with indicated doses of **MGD-4**, **MGD-28** or pomalidomide (Pom) for 3 days, and cells were stained with Annexin V-PE and DAPI (**A**). Apoptosis was measured by flow cytometry using Annexin V as a marker (**B**). Error bars denote standard deviations (independent experiments, $n = 3$). Student's t test, ns (no significance), $^{**}p < 0.01$. **C**. Viability of wild type and CRBN$^{-/-}$ NCI-H929 cells treated with **MGD-28** for 96 h. Data shown are a representative graph of three independent experiments; mean ± SD of triplicates. **D**. MV-4-11 cells viability in the absence and presence of pomalidomide (Pom, 10 μM) for 96 h. Data shown are a representative graph of three independent experiments; mean ± SD of triplicates. **E**. Western blot analysis of CK1α, IKZF1, IKZF2 and IKZF3 degradation in NCI-H929 cells CRBN knockout, pre-treated with MLN4924, MG132 or pomalidomide for 1 h and treated with **MGD-28** for 24 h. **F**. Western blot analysis of p53, p21 and MDM2 in NCI-H929 cells treated with different doses of **MGD-28** for 24 h. **G-H**. PCR analysis of CDKN1A/p21 (**G**) and MDM2 (**H**) in MV-4-11 cells treated with different doses of **MGD-28**, lenalidomide (Len, 10 μM) or pomalidomide (Pom, 10 μM) for 24 h. Error bars denote standard deviations (independent experiments, $n = 3$). Student's t test, ns (no significance), $^{**}p < 0.01$. **I**. Western blot analysis of CK1α, p53, and p21 in NCI-H929 cells overexpressing CK1α WT, CK1α G40N, or vector control treated with lenalidomide (Len, 10 μM) or **MGD-28** (1 μM). **J**. NCI-H929 cells overexpressing CK1α WT, CK1α G40N, or vector were treated with **MGD-28**. Data shown are a representative result of three independent experiments; mean ± SD of triplicates.

accompanied by depletion of CK1α at concentrations as low as 1–10 nM in NCI-H929, MV-4-11, and WSU-DLCL-2 cells, as demonstrated in the immunoblot analyses of endogenous proteins (Fig. 3F and Fig. S4C). This depletion was which was much more efficient than that observed for **MGD-4** or lenalidomide. Notably, **MGD-28** also exhibited significant degradation of IKZF1 (DC_{50}=3.8 nM, D_{max} = 94.1%), IKZF2 (DC_{50}=56.3 nM, D_{max} = 83.3%), and IKZF3 (DC_{50}=7.1 nM, D_{max} = 90.7%). Treatment with 1 μM **MGD-28** for 4 h significantly reduced IKZF1 and IKZF2 by over 60%, and IKZF3 by over 80% (Fig. 3G and H), and potent endogenous degradation of IKZF1, IKZF2, and IKZF3 by **MGD-28** was observed in the NCI-H929, MV-4-11, and WSU-DLCL-2 cells (Fig. 3I and Fig. S4D). Similar to lenalidomide and pomalidomide, **MGD-4** and **MGD-28** also exhibited minimal effects on CRBN expression (Fig. S4E, **S4F**). Moreover, **MGD-28** inhibited the growth of a panel of hematological cancer cell lines, with IC_{50} values ranging from single-digit nanomolar to submicromolar concentrations, and showed markedly reduced toxicity on PBMCs derived from healthy donors, with an IC_{50} value exceeding 10 μM (Fig. 3J and Fig. S4G). Furthermore, treatment with **MGD-28** at concentrations of 10 and 100 nM resulted in significant dose-dependent induction of apoptosis after three days in NCI-H929, MV-4-11, and WSU-DLCL-2 cells (Fig. 3K, Fig. S4H). These results demonstrate that **MGD-28** exhibited high antiproliferative potency and a significant degradation effect towards Ikaros family neosubstrates and CK1α.

MGD-28 exhibited a significant degradation effect on IKZF1/2/3 and CK1α via a Cullin-CRBN dependent pathway

After identifying **MGD-4** and **MGD-28** as potent antiproliferative and degrading agents, we investigated whether this effect depended on CRBN. We initially conducted a cell viability assay using wild-type and CRBN knockout (CRBN$^{-/-}$) NCI-H929 cells. In contrast to the effects in wild-type NCI-H929 cells, neither **MGD-4** nor **MGD-28** induced apoptosis in CRBN$^{-/-}$ NCI-H929 cells (Fig. 4A and B and Fig. S5A). Furthermore, the antiproliferative effects of **MGD-28** were significantly reduced in CRBN$^{-/-}$NCI-H929 cells (Fig. 4C), confirming that the mechanism of action is CRBN dependent. To validate this hypothesis, we performed ligand competition experiments in MV-4-11 cells. The cells were treated with varying doses of **MGD-28** in the presence of high concentrations of pomalidomide (10 μM). Excess pomalidomide saturated the CRBN-binding site, rendering it inaccessible to other CRBN modulators and abrogating the antiproliferative and degradation effects of **MGD-28** (Fig. 4D and E). In addition, CRBN knockout and cotreatment with MLN4924 (a NEDD8-activating enzyme inhibitor), the proteasome inhibitor MG132, or pomalidomide prevented the degradation of substrates. This observation suggests that the degradation process depends on a Cullin-CRBN dependent pathway (Fig. 4E and Fig. S5B). For Immunoblot analysis, NCI-H929 and MV-4-11 cells were treated with cyclohexamide (CHX, 100 μg/mL) for the indicated periods, and the cells were pretreated with dimethyl sulfoxide or **MGD-28** for 30 min. As shown in Figure S5C, **MGD-28** decreased the protein half-life of CK1α and IKZF1/2/3, indicating that **MGD-28** promotes multiple neosubstrates destruction.

CK1α regulates the stability of MDM2/MDM4 and TP53 [18]. Therefore, we further investigated the effects of **MGD-28** on the p53-regulated pathway. Treatment with increasing doses of **MGD-28** significantly increased the protein levels of p53, CDKN1A/p21, and MDM2 after 48 h in both NCI-H929 and MV-4-11 cells, as well as increased the mRNA levels of p21 and MDM2 (Fig. 4F and G and Fig. S5D-S5F), indicating that **MGD-28** activates the p53 pathway by degrading CK1α. We next utilized the degradation-resistant mutant CK1α^{G40N}, which cannot engage lenalidomide-bound CRL4^{CRBN} [38]. As shown in Fig. 4I and Figure S5G, **MGD-28** and lenalidomide could not degrade the CK1α^{G40N} mutant, which blocked the upregulation of p53 and p21. Furthermore, cells expressing the CK1α^{G40N} mutation showed a significantly reduced response to **MGD-28** and lenalidomide compared with cells containing the vector or wild type CK1α (Fig. 4J and Fig. S5H, S5I), confirming that **MGD-28** mediated degradation of CK1α contributes to its antiproliferative effect.

MGD-28 exhibited high efficiency in MM tumor xenograft with favorable pharmacokinetic properties

In vivo studies were conducted to further examine the efficacy of **MGD-4** and **MGD-28** in BALB/c nude mice bearing MM xenograft tumors. These studies were based on the exceptionally potent antiproliferative and degradation effects observed in vitro. The pharmacokinetic (PK) properties of **MGD-4** and **MGD-28** were also evaluated. Following a single intravenous (*i.v.*) administration at dose of 1 mg/kg, we observed low to medium clearance values and distribution volume values of 1.91 and 5.79 L/h/kg, 1.73 and 10.22 L/kg in rats for **MGD-4** and **MGD-28**, respectively. These PK parameters indicate satisfied the exposure and limited distribution beyond the circulation compartment. Following a single oral dose of 3 mg/kg, the times to peak plasma concentrations were approximately 0.3 and 0.7 h for **MGD-4** and **MGD-28**, respectively, suggesting rapid absorption. Furthermore, the favorable oral bioavailability values of **MGD-4** and **MGD-28** were 82.5% and 36.7%, respectively (Fig. 5A and Fig. S6A).

Based on the overall PK profile of the degraders, a pharmacodynamic study was conducted involving oral route of administration and two dosing regimens: 3 and 10 mg/kg once per day (Fig. 5B). As illustrated in Fig. 5C, compared with the vehicle, daily oral administration of **MGD-4** and **MGD-28** at a dose of 3 mg/kg resulted in tumor growth inhibition (TGI%) values of 66.5% and 85.5%, respectively, after 10 days of treatment in NCI-H929 xenograft tumors. Higher doses of **MGD-4** (10 mg/kg) significantly inhibited tumor growth, with a TGI% value of 92.8%, which surpassed that of pomalidomide (80.1%, 10 mg/kg). A higher dose of **MGD-28** (10 mg/kg) led to tumor regression, as reflected by the smaller tumor volume compared with that on the initial day. As the administration period was extended from 10 to 18 days, the difference in antitumor efficacy between the same doses of pomalidomide, **MGD-4**, and **MGD-28** became more pronounced. By day 18, the volume of the pomalidomide (10 mg/kg) group reached approximately 1500 mm^3, whereas the **MGD-4** (10 mg/kg) and **MGD-28** (3 mg/kg) groups achieved approximately half the tumor volume compared with the pomalidomide group. Moreover, **MGD-28** (10 mg/kg) demonstrated consistent inhibitory effects with complete tumor regression. Furthermore, **MGD-4** (10 mg/kg) and **MGD-28** (10 mg/kg) were well tolerated in nude mice, as indicated by slight weight loss during the treatment period (Fig. 5D). Immunohistochemical (IHC) sections of the tumors were stained with Ki67. In accordance with the TGI studies, the **MGD-4** and **MGD-28** groups exhibited a notable reduction in the percentage of Ki67-positive tumor cells at single doses of 3 and 10 mg/kg (Fig. 5E). Furthermore, we conducted western blot analysis of CRBN, CK1α, IKZF1, IKZF2 and IKZF3 in harvested tumors from mice treated with in NCI-H929 tumor xenograft. As shown in Fig. 5F, in consistent with the in vitro studies, **MGD-4** (3, 10 mg/kg) and **MGD-28** (3, 10 mg/kg) groups significantly reduced the levels of IKZF1, IKZF2 and IKZF3 in tumor issues, which showed more pronounced degradation effect than pomalidomide. Notably, **MGD-28** (3, 10 mg/kg) dramatically reduced the level of CK1α, whereas **MGD-4** and pomalidomide showed minimal efficacy on reducing CK1α protein, corroborating their efficacious degradation effects in vivo.

Synergetic effect of MGD-4/MGD-28 with standard therapeutic agents in inhibiting MM tumor growth

Several studies demonstrated that a combination of IMiDs and immunosuppressive steroids markedly enhances overall survival rates in the treatment of MM. Furthermore, combining IMiDs with proteasome inhibitors and EZH2 inhibitors has become the standard of care for both newly diagnosed and relapsed/refractory patients with MM [39, 40], emphasizing the advantages of a multi-targeted therapeutic strategy for MM and AML. The initial investigation involved examining the combinational efficacy of our degraders with the immunosuppressive steroid dexamethasone. As shown in Fig. 6A, dexamethasone (3 mg/kg) only modestly inhibited tumor growth when used as a single agent in the NCI-H929 xenograft model, with a TGI% of 43.7% at 10 days' post-treatment. However, when combined with the degrader **MGD-4** (3 mg/kg), the tumor size was significantly reduced compared with that after monotherapy, with a TGI% of 90.21%. Similarly, the combination of dexamethasone and **MGD-28** (3 mg/kg) demonstrated significant effects with a TGI% of 99.2%. The pronounced inhibitory effects of the dexamethasone+**MGD-4** and dexamethasone+**MGD-28** combinations were sustained throughout the continuous treatment period, and there were no discernible signs of body weight loss or other toxic effects at the applied doses (Fig. 6B). Moreover, immunohistochemical analysis of Ki67-stained tumor sections revealed that combination treatment exhibited a more pronounced inhibitory effect on the number of Ki67-positive cells, confirming efficacy of the combination (Fig. 6C).

The combination effects of the EZH2 inhibitor tazemetostat and proteasome inhibitor bortezomib on the degrader **MGD-28** were also investigated. Daily administration of tazemetostat (100 mg/kg) as a single agent had a minimal effect on tumor growth. However, its combination with **MGD-28** (3 mg/kg) led to a TGI% of 95.8%, whereas twice-weekly administration of bortezomib (1 mg/kg) as monotherapy had a limited TGI% of 29.9%. In contrast, the combination of bortezomib and **MGD-28** showed profound effects and resulted in tumor regression

A

Parameter	unit	MGD-4		MGD-28	
		i.v.	p.o.	i.v.	p.o.
$t_{1/2}$	h	3.73 ± 1.36	3.93 ± 0.75	1.67 ± 0.27	1.96 ± 0.11
C_0	ng/mL	1583 ± 248.4	/	463.1 ± 92.26	/
C_{max}	ng/mL	/	1137 ± 339.9	/	127.9 ± 121.6
T_{max}	h	/	0.29 ± 0.10	/	0.71 ± 0.33
$AUC_{(0-t)}$	h·μg/mL	814.1 ± 90.37	2016 ± 257.9	411.7 ± 85.56	452.7 ± 349.4
$AUC_{(0-inf)}$	h·μg/mL	826.9 ± 88.23	2084 ± 202.0	415.1 ± 86.89	463.0 ±350.3
V_{ss}	L/kg	1.73 ± 0.18	/	10.22 ± 2.97	/
CL	L/h/kg	1.91 ± 0.15	/	5.79 ± 1.05	/
$MRT_{(0-inf)}$	h	0.90 ± 0.09	1.98 ± 0.62	1.75 ± 0.28	6.98 ± 3.62
F	%	/	82.5 ± 10.6	/	36.7 ± 2.83

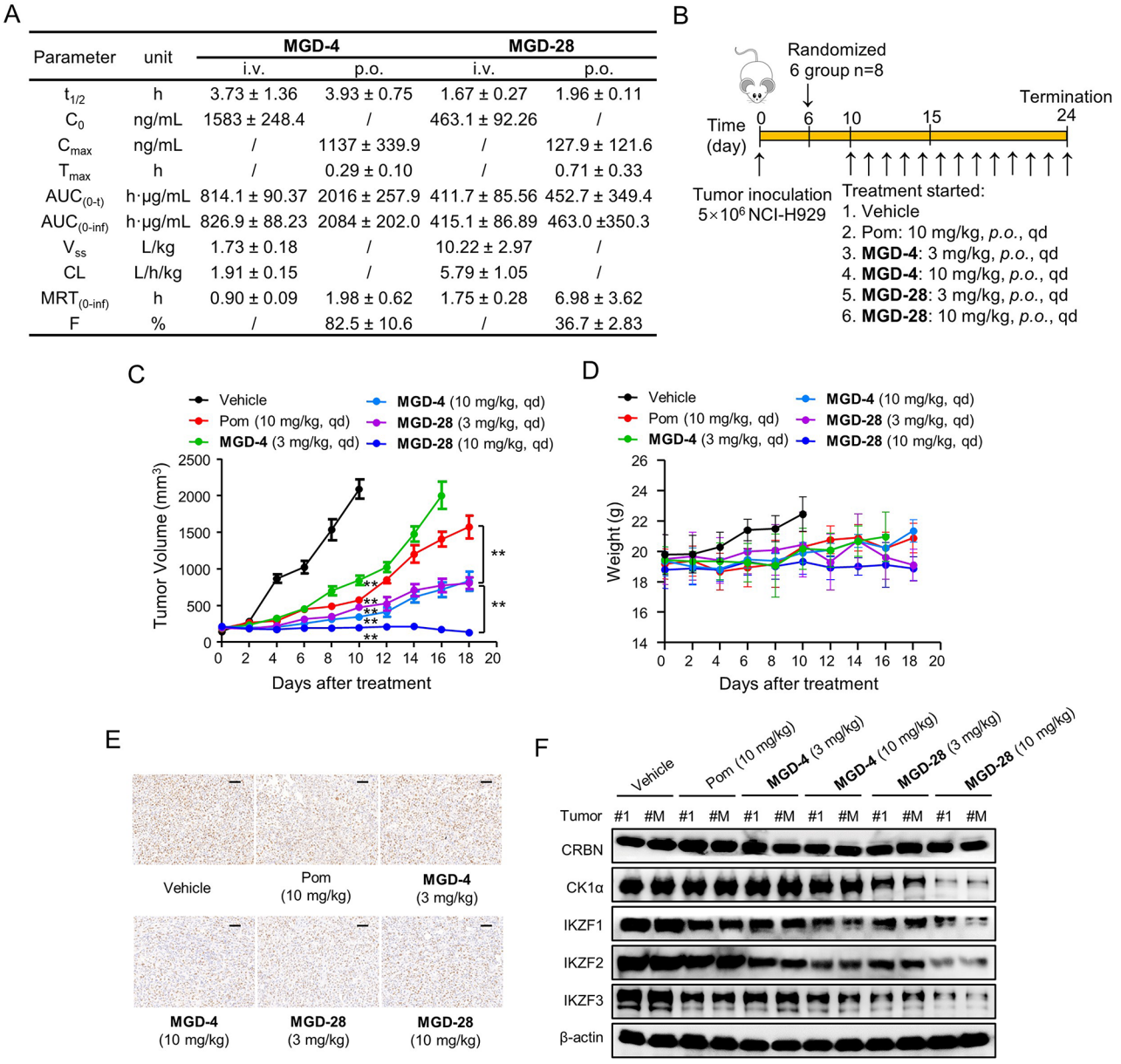

Fig. 5 MGD-28 exhibited high efficiency in MM tumor xenograft with favorable pharmacokinetic properties. **A**. The mean pharmacokinetic parameter in rats for **MGD-4** and **MGD-28** obtained after intravenous (*i.v.*) and oral administration (*p.o.*) (mean ± SD, $n = 6$). **B**. Treatment schedule for the NCI-H929 cells xenograft tumors model treated with vehicle, pomalidomide, **MGD-4** and **MGD-28**, respectively. **C**-**D**. BALB/c nude mice transplanted with NCI-H929 cells were orally administrated vehicle control, pomalidomide (Pom), **MGD-4**, or **MGD-28** with single doses of 3 mg/kg or 10 mg/kg for 18 days. The change of NCI-H929 tumor volume (**D**) and change of body weight (**E**) of all mice in each group were shown ($n = 8$). Data are shown as mean ± SD, $^{**}p < 0.01$ (one-way ANOVA). **E**. Representative images of Ki67-IHC staining in harvested tumors from each group in (**B**) are shown. Scale bars represent 50 mm. **F**. Western blot analysis of CRBN, CK1α, IKZF1, IKZF2 and IKZF3 in harvested tumors or their mixture (#M, $n = 8$) from each group were shown

(Fig. 6D and E). The final tumor weight further validated the efficacy of these combinations (Fig. 6F), and the single agent and drug combinations groups exhibited no discernible toxicity at the doses employed, as evidenced by minimal fluctuations in body weight throughout the experiment (Fig. 6G). Moreover, the weights of the major organ (heart, lung, liver, stomach, and double kidney), as well as routine blood parameters of the mice (leukocyte, red blood cell, hemoglobin and platelet count) in the mice in each drug treatment group did not significantly differ from those in the control group (vehicle), indicating minimal toxicity to mice overall and at the organ level (Fig. S6B, S6C and Table S2). Furthermore, immunohistochemical analysis of Ki67-stained tumor sections revealed a smaller number of Ki67-positive cells in the combination groups, providing further evidence of their

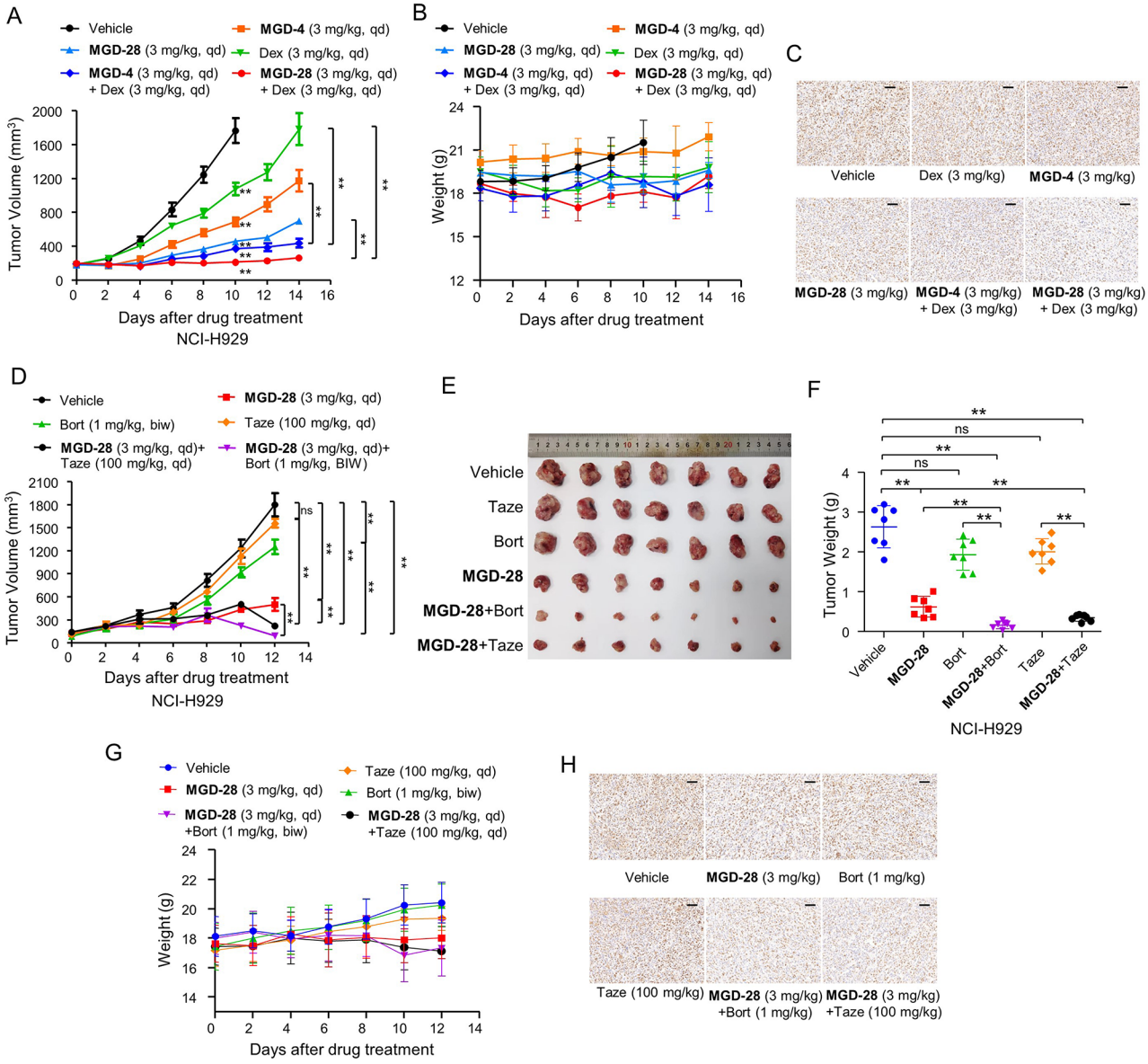

Fig. 6 Synergetic effect of MGD-4/MGD-28 with standard therapeutic agents in inhibiting MM tumor growth. **A-B.** BALB/c nude mice transplanted with NCI-H929 cells were orally administrated with single agent dexamethasone (Dex), **MGD-4**, **MGD-28** and vehicle as well as combinational treatment of Dex + **MGD-4** and Dex + **MGD-28** for 14 days. The change of NCI-H929 tumor volume (**A**) and change of body weight (**B**) of all mice in each group were shown ($n = 8$). Data are mean ± SD, ns (no significance), $^{**}p < 0.01$ (one-way ANOVA). **C**. Representative images of Ki67-IHC staining in harvested tumors from each group in (**A**) are shown. Scale bars represent 50 mm. **D**-**G**. NOD/SCID nude mice transplanted with NCI-H929 cells were orally administrated with single agent bortezomib (Bort), **MGD-28**, tazemetostat (Taze) and vehicle as well as combinational treatment of Bort + **MGD-28** and Taze + **MGD-28** for 12 days. The change of NCI-H929 tumor volume (**D**), tumors' picture (**E**), tumor weight (**F**) and change of body weight (**G**) of all mice in each group were shown ($n = 7$). Data are mean ± SD, ns (no significance), $^{**}p < 0.01$ (one-way ANOVA). **H**. Representative images of Ki67-IHC staining in harvested tumors from each group in (**D**) are shown. Scale bars represent 50 mm

significant inhibitory effects on NCI-H929 tumor growth (Fig. 6H). Collectively, these results indicate that the combination of **MGD-4**/**MGD-28** with a standard therapeutic agent had a pronounced synergistic effect, demonstrating its potential as a therapeutic approach for MM.

Proteomics analysis showed that MGD-4/MGD-28 exerted multiple neosubstrates degradation

Several studies have demonstrated that IMiDs facilitate a range of pharmacological activities by specifically degrading various neosubstrates in a variety of contexts [1, 4]. To further investigate the global protein degradation of neosubstrates induced by our degraders, we performed quantitative proteomics analysis in

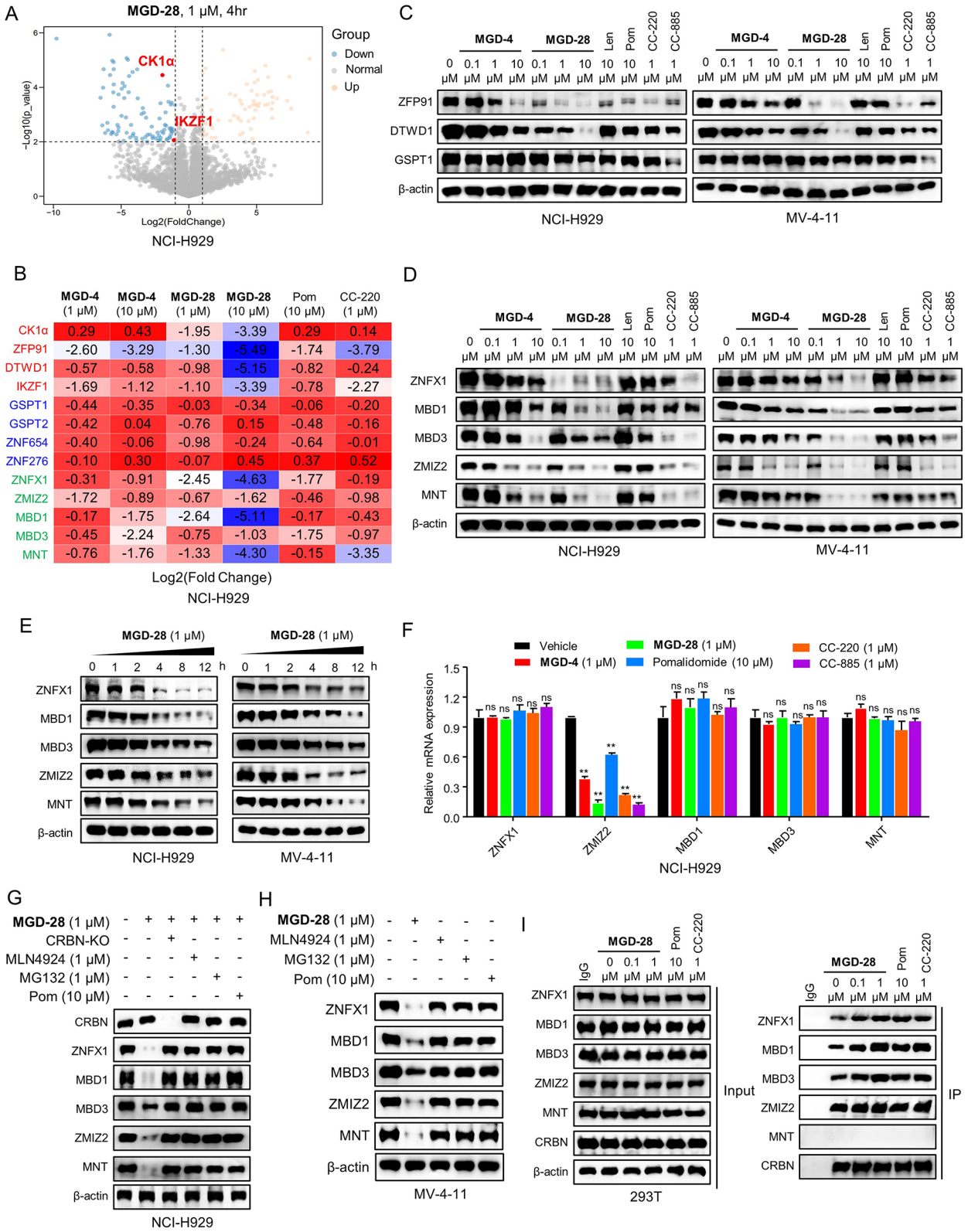

Fig. 7 (See legend on next page.)

(See figure on previous page.)

Fig. 7 Proteomics analysis showed that MGD-4/MGD-28 exerted multiple neosubstrates degradation. **A**. TMT-labelled quantitative global proteomics analysis of NCI-H929 cells treated for 4 h with **MGD-28** (1 μM). **B**. Heatmap showing the ratio of global neosubstrates in whole-proteome quantification. NCI-H929 cells were treated with DMSO, **MGD-4** (1 μM, 10 μM), **MGD-28** (1 μM, 10 μM), pomalidomide (Pom, 10 μM) and CC-220 (1 μM) for 4 h; quantitative proteomics analysis was performed using label-free quantitative intensities (biological replicates, $n = 3$). Source data are provided as a source data file. **C**. Western blot analysis of neosubstrates including ZFP91, DTWD1 and GSPT1 in NCI-H929 and MV-4-11 cells treated with the indicated compound for 24 h. **D**. Western blot analysis of ZNFX1, MBD1, MBD3, ZMIZ2 and MNT in NCI-H929 and MV-4-11 cells treated with the indicated compound for 24 h. **E**. Western blot analysis of ZNFX1, MBD1, MBD3, ZMIZ2 and MNT in NCI-H929 and MV-4-11 cells treated with **MGD-28** (1 μM) at indicated time. **F**. qPCR analysis ZNFX1, MBD1, MBD3, ZMIZ2 and MNT in NCI-H929 cells treated with **MGD-4** (1 μM), **MGD-28** (1 μM), pomalidomide (10 μM), CC-220 (1 μM) and CC-885 (1 μM) for 24 h. Error bars denote standard deviations (independent experiments, $n = 3$). $^{**}p < 0.01$ (t-test). **G**. Western blot analysis of ZNFX1, MBD1, MBD3, ZMIZ2 and MNT expression in NCI-H929 cells CRBN knockout, pre-treated with MLN4924, MG132 or pomalidomide (Pom) for 1 h and treated with **MGD-28** (1 μM) for 24 h. **H**. Western blot analysis of ZNFX1, MBD1, MBD3, ZMIZ2 and MNT expression in MV-4-11 cells pre-treated with MLN4924, MG132 or pomalidomide for 1 h and treated with **MGD-28** (1 μM) for 24 h. **I**. Immunoprecipitation of ZNFX1, MBD1, MBD3, ZMIZ2 and MNT in NCI-H929 cells treated with DMSO, **MGD-28** (0.1, 1 μM), pomalidomide (Pom, 10 μM) and CC-220 (1 μM) for 2 h

NCI-H929 cells treated with **MGD-4** (10 μM), **MGD-28** (10 μM), pomalidomide (10 μM), and CC-220 (1 μM) for 4 h (Fig. 7A and Fig. S7A, S7B). In accordance with the results of in vitro studies, CK1α was significantly reduced (approximately 75% and 91%) by **MGD-28** at 1 and 10 μM, respectively, but not by **MGD-4** and pomalidomide. Neosubstrates, including ZFP91, DTWD1, and IKZF1, were significantly reduced in response to **MGD-4**, **MGD-28**, and pomalidomide, whereas other neosubstrates such as GSPT1, GSPT2, ZNF654, and ZNF276, were not affected (Fig. 7B). To validate the proteomic findings, we performed immunoblot analysis of **MGD-4**, **MGD-28** and IMiDs (lenalidomide, pomalidomide, CC-220 and CC-885) in NCI-H929 and MV-4-11 cells. In agreement with previous studies, ZFP91 and DTWD1 were degraded by pomalidomide, CC-122, and CC-885, which were also significantly reduced by **MGD-4** and **MGD-28** at submicromolar concentrations. This result demonstrates the ability of **MGD-4** and **MGD-28** to degrade multiple neosubstrates along with their higher potency compared with lenalidomide and pomalidomide. Moreover, except CC-885, these molecules did not degrade GSPT1 (Fig. 7C).

To determine other potential mechanisms underlying the antiproliferative efficacy of **MGD-4** and **MGD-28**, we further investigated other potential targets. Transcription factors (ZFs) remain challenging drug targets because of the absence of druggable active sites [41]. Comprehensive mapping of the ZFs library of differentially expressed proteins revealed that 78 ZFs were overlapped. Transcription factors such as ZNFX1, ZMIZ2, MBD1, MBD3, and MNT, were significantly reduced after **MGD-4** and **MGD-28** treatment. Pomalidomide exhibited less pronounced effects in reducing the ZMIZ2, MBD1 and MNT protein abundance, but significantly decreased the levels of ZNFX1 and MBD3. CC-220 significantly reduced the levels of ZMIZ2, MBD3, and MNT, while exhibiting moderate effects on the ZNFX1 and MBD1 protein abundance (Fig. 7B). These findings prompted us to conduct further validation studies.

First, as shown in Fig. 7D, immunoblot analyses demonstrated that endogenous ZNFX1, MBD1, MBD3, ZMIZ2 and MNT proteins were dose-dependently reduced by **MGD-4** and **MGD-28** in NCI-H929 and MV-4-11 cells. Furthermore, CC-220 and CC-885 exhibited significant degradation effects, whereas lenalidomide and pomalidomide showed minimal or slight effects. Time-dependent experiments demonstrated that the degradation effect of **MGD-28** on ZNFX1, MBD1, MBD3, ZMIZ2 and MNT was enhanced by prolonging the incubation time (Fig. 7E). Second, neither degraders (**MGD-4** and **MGD-28**) nor IMiDs (pomalidomide, CC-220, and CC-885) decreased the mRNA levels of ZNFX1, MBD1, MBD3, and MNT, suggesting the involvement of a non-transcriptional regulatory mechanism. In contrast, the mRNA expression of ZMIZ2 was reduced by **MGD-4**/**MGD-28**, pomalidomide, CC-220, and CC-885 treatments, indicating the involvement of a transcriptional mechanism (Fig. 7F and Fig. S7C). CRBN knockout, addition of MLN4924, and the proteasome inhibitor MG-132 prevented the degradation of ZNFX1, MBD1, MBD3, ZMIZ2, and MNT in the presence of **MGD-28** (Fig. 7G and H). Finally, we evaluated the capacity of these proteins to interact with CRBN following **MGD-28** or IMiD treatment. We observed increased levels of endogenous ZNFX1, MBD1, and MBD3 that co-immunoprecipitated with CRBN in the presence of **MGD-28**, pomalidomide, and CC-220. In contrast, co-immunoprecipitation of endogenous ZMIZ2 did not change, and no co-immunoprecipitation of endogenous MNT was observed with CRBN (Fig. 7I). This result indicates that **MGD-28** leads to CRBN-dependent ubiquitination and the subsequent proteasomal degradation of ZNFX1, MBD1 and MBD4. These findings demonstrate that **MGD-4** and **MGD-28** induce the degradation of multiple neosubstrates to exert anti-MM and anti-leukemia effects.

MGD-28 has profound cytotoxic activity in different stage of MM cells and shows a broad antiproliferative profile

MM exhibits no obvious symptoms in the early stages, whereas advanced stages are characterized by injury to the bone system and represent a severe threat to human health, and the prognosis of patients with distal metastasis (extra-bone MM, at an advanced disease

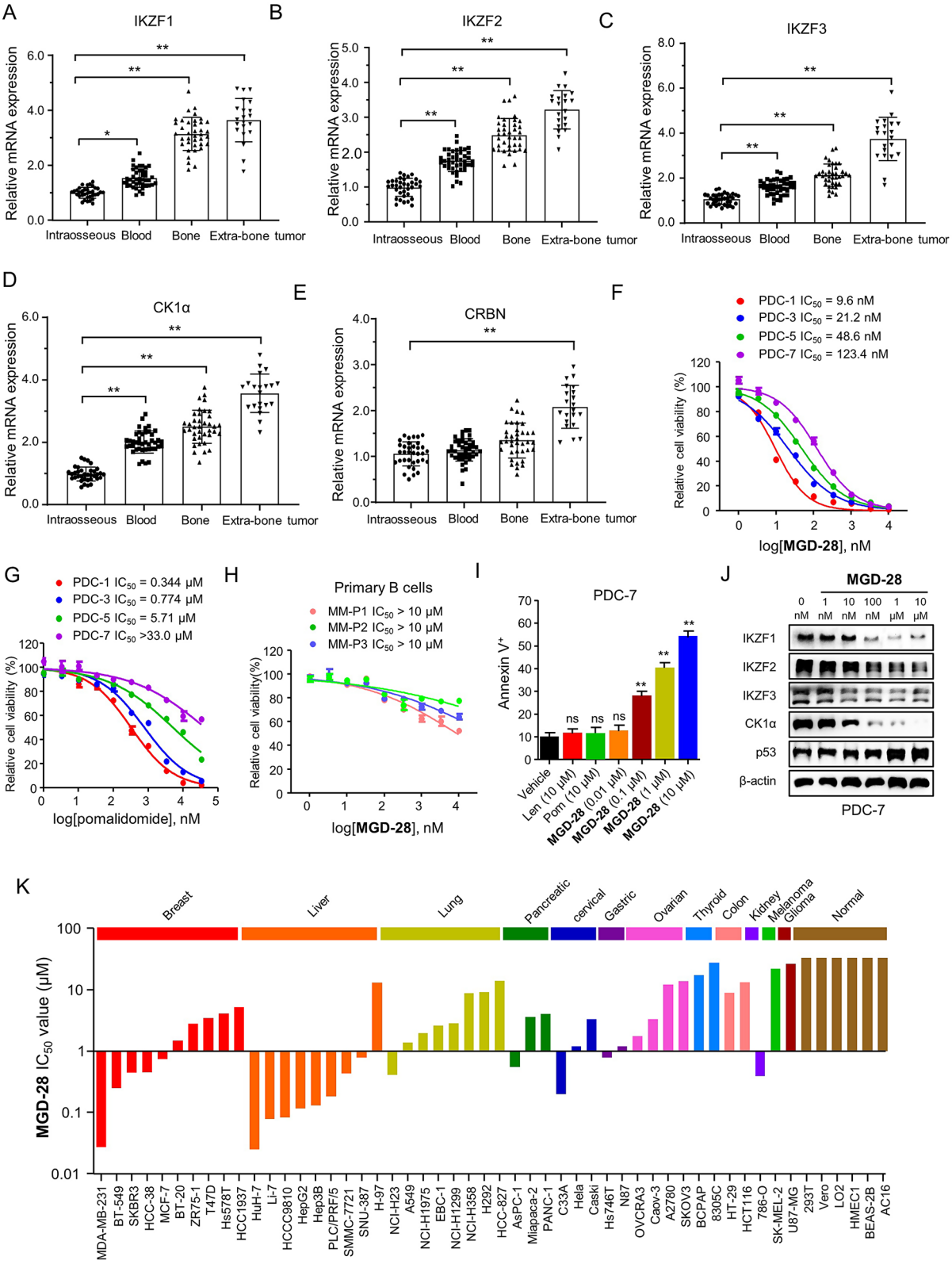

Fig. 8 (See legend on next page.)

(See figure on previous page.)

Fig. 8 MGD-28 has profound cytotoxic activity in different stage of MM cells and shows a broad antiproliferative profile. **A**-**E**. The expression level of IKZF1 (**A**), IKZF2 (**B**), IKZF3 (**C**), CK1α (**D**) and CRBN (**E**) in MM specimens at different stages. * $p < 0.05$, ** $p < 0.01$. **F-G**. Viability assay of four MM PDCs (1, 3, 5, or 7) treated with **MGD-28** (**F**) or pomalidomide (**G**) for 4 days. Data shown are a representative graph of three independent experiments; mean ± SD of triplicates. **H**. Viability assay of primary B cells obtained from the 3 MM patients (MM-P1. MM-P2 and MM-P3) treated with **MGD-28** for 4 days. Data shown are a representative graph of three independent experiments; mean ± SD of triplicates. **I**. Flow cytometry plot showing PDC-7 treated with indicated compounds for 3 days, stained with Annexin V-PE and DAPI. Histograms show the relative cell percentage of apoptosis in PDC-7. Error bars denote standard deviations (independent experiments, $n = 3$). Student's t test, ns (no significance), ** $p < 0.01$. **J**. Western blot analysis of PDC-7 treated with different concentrations of **MGD-28** for 24 h. **K**. IC_{50} values of **MGD-28** for the 46 solid cancer cell lines and 6 normal cell lines relative to the panel average IC_{50}

stage) remains poor [2]. Thus, we investigated the effect of **MGD-28** on different stages of MM cells. First, the expression of CBRN, IKZF1, IKZF2, IKZF3 and CK1α in MM clinical specimens was examined using qPCR, respectively. As shown in Fig. 8A and D, the expression level of IKZF1, IKZF2, IKZF3 and CK1α in intraosseous samples was significantly lower than that in the other three MM specimens, and highest in extra-bone tumor samples. In clinical specimens from all 4 stages, the expression of these factors increased with disease progression. Although the expression level of CBRN was similar among intraosseous samples, blood and bone tumor samples, its expression in extra-bone tumor samples was significantly increased (Fig. 8E), indicating the essential roles of these factors in MM progression. Next, we evaluated the antiproliferative effect of **MGD-28** on various stage of MM patient-derived cell (PDC) lines including PDC-1 (intraosseous MM), PDC-3 (MM cells separated from patients' blood), PDC-5 (MM cells separated from the tumor tissues in bone) and PDC-7 (Extra-bone tumor). As shown in Fig. 8F and G, MM PDCs showed a gradual decrease in their sensitivity to **MGD-28** and pomalidomide with disease progression. **MGD-28** efficiently reduced the survival of the four PDC lines of MM cells, with IC_{50} values range from the digit nanomolar to submicormolar levels; these effects were approximately 100-fold stronger than that of pomalidomide. Notably, **MGD-28** showed much lower activity against normal primary B cells obtained from the three patients with MM (Fig. 8H). Similarly, both **MGD-4** and **MGD-28** demonstrated minimal effect on normal primary B cells obtained from two healthy individuals, with IC_{50} values over 10 μM (Fig. S8A, **S8B**). Furthermore, **MGD-28** significantly induced PDC-7 apoptosis in a dose-dependent manner, exhibiting much higher potency than the minimal effects of lenalidomide and pomalidomide (Fig. 8I). In addition, endogenous IKZF1, IKZF2, IKZF3, and CK1α were effectively degraded following **MGD-28** treatment 100 nM (Fig. 8J).

Given that **MGD-28** degradedIKZF1/2/3 and CK1α, we assessed whether it possessed broad spectrum or selective antiproliferative effects across a diverse range of human cancers, including 46 human solid cancer cell lines. Remarkably, **MGD-28** potently inhibited the viability of multiple cell lines derived from solid tumors, such as breast and liver cancer cells, with IC_{50} values ranging from double-digit nanomolar to single-digit micromolar levels (Fig. 8K). Thus, **MGD-28** shows potential as a treatment option for a broad spectrum of hematological and solid tumors. In contrast, six normal cell lines from different tissues were insensitive to **MGD-28** ($IC_{50} > 33$ μM), highlighting the high selectivity of **MGD-28** toward cancer cell lines.

BRD9 activation mediates acquired resistance to IMiDs

Despite the significant improvement in the outcomes of patients with MM treated with IMiDs, patients develop resistance to these agents, frequently resulting in disease relapse. In addition, cell lines with acquired resistance have been employed in drug screening efforts to identify more potent CRBN binders that may overcome the resistance to existing IMiDs. We constructed NCI-H929 and RPMI-8226 cells with acquired resistance to lenalidomide and pomalidomide, respectively. The IC_{50} values in these cells were increased by more than 10-fold compared with those in primary cells (Fig. S9A-S9D). **MGD-28** retained its potent inhibitory efficacy at concentrations in the double-digit nanomolar to submicromolar range. Next, we examined the expression of CRBN and its substrates. Both cell lines exhibited comparable expression levels of substrates (IKZF1, IKZF2, IKZF3, and CK1α) and slightly decreased expression of CRBN (Fig. S9E-S9G). This result indicates that resistance is not associated with abnormalities in CRBN or its associated neosubstrates and may instead be caused by activation of alternative pro-survival pathways.

To further elucidate the mechanisms underlying IMiDs resistance, we conducted proteomics analyses in MM cells with acquired resistance to IMiDs, which enabled comprehensive assessment of protein changes. The analysis revealed significantly increased expression of bromodomain-containing protein 9 (BRD9) in both lenalidomide/pomalidomide-resistant NCI-H929 ($NCI\text{-}H929^{Len-R}$/$NCI\text{-}H929^{Pom-R}$) cells (Fig. 9A and Fig. S10A). The protein and mRNA levels of BRD9 were increased in resistant cells. As an essential component of the SWI/SNF chromatin remodeling complex, studies have demonstrated that BRD9 uses its bromodomain to stimulate c-Myc expression and AML cell proliferation. Given that BRD9 negatively regulates SOCS3 expression, BRD9 may influence activation of the tumor-driver STAT5 pathway and affects leukemic cell proliferation

and survival [42, 43]. Furthermore, we observed a significant increase in the protein and mRNA levels of c-Myc and STAT5 associated with BRD9 (Fig. 9B and C). We next investigated the effects of BRD9-mediated resistance to IMiDs. First, we evaluated whether inhibition of BRD9 using I-BRD9, a highly selective BRD9 inhibitor, could overcome IMiDs resistance. Addition of I-BRD9 successfully overcame the resistance and mediated synergistic cytotoxicity with pomalidomide and lenalidomide in the corresponding IMiDs-resistant NCI-H929 and RPMI-8226 cells (Fig. 9D and Fig. S10B). In addition, overexpression of BRD9 resulted in strong resistance of MM cells (RPMI-8226, NCI-H929, and OPM-2), as evidenced by an approximately 5-6-fold increase in the IC_{50} values for pomalidomide-induced cell death (Fig. 9E and F and Fig. S10C-S10E). Moreover, the combination of I-BRD9 and pomalidomide induced cytotoxic effects in wild-type NCI-H929, MV-4-11, and WSU-DLCL-2 cells, as evidenced by the highest single-agent (HAS) model, with a synergy score exceeding 10. Similar results were obtained for I-BRD9 and **MGD-28** (Fig. 7G and H and Fig. S10F-S10I).

The efficacy of combination treatment in overcoming IMiDs resistance in vivo was assessed. As illustrated in Fig. 9I and J, single-agent treatment with pomalidomide (10 mg/kg, *p.o.*) had a minimal effect compared with that of the vehicle, indicating that the reserved resistance of NCI-H929^{Pom-R} cells to pomalidomide in vivo. However, daily oral administration of I-BRD9 (10 mg/kg) as a single agent resulted in a modest TGI% of 47.8% with 18 days post-treatment. In contrast, when I-BRD9 was combined with pomalidomide, the tumor growth of NCI-H929^{Pom-R} cells was significantly reduced, with a TGI% of 82.3%. This result suggests that BRD9 inhibitors can overcome IMiDs resistance in vivo by inhibiting BRD9 activation. In accordance with the findings of in vitro studies, oral administration of **MGD-28** at a dose of 3 mg/kg daily potently inhibited tumor growth, with a TGI% of 71.9%. Furthermore, the combination of I-BRD9 (10 mg/kg) and **MGD-28** (3 mg/kg) resulted in a more profound inhibitory effect with a TGI% of 93.6%. The drug combination exhibited a consistent and potent inhibitory effect on tumor growth. Neither drug combinations caused discernible toxicity at the administered doses, as indicated by slight fluctuations in body weight observed during the experiment. Furthermore, IHC sections of tumors stained with Ki67 revealed a more pronounced inhibitory effect on the number of Ki67-positive cells in the combination group, confirming the strong inhibitory effect on IMiDs-resistant MM tumor growth (Fig. 9K). Our findings indicated that BRD9 activation is a pivotal factor in the regulation of IMiDs sensitivity. Furthermore, BRD9 inhibition may restore IMiDs-induced MM cytotoxicity and enhance the anti-leukemic effects of IMiDs against MM and AML.

Synergy between BRD9 inhibitors and IMiDs as a therapeutic strategy for MM

Next, we validated the potential of co-targeting with a BRD9 inhibitor and CRBN for clinical MM treatment. First, the expression of BRD9 in MM clinical specimens was examined using qPCR. As shown in Fig. 10A, the expression of BRD9 was significantly lower in intraosseous samples than in the other three MM specimens, and highest in extra-bone tumor samples, demonstrating that BRD9 is involved in tumor development and progression. Second, the expression level of BRD9 was positively related to the expression of IKZF1, IKZF2, IKZF3, and CK1αin MM specimens at different stages; the results are shown in a scatter plot with P values (Fig. 10B and E). Third, the dose-response curve for I-BRD9 combined with **MGD-28** revealed much higher potency than a single agent and strong synergistic effects on PDC-7 viability, as evidenced by the HAS model with a synergy score of 11.93 (Fig. 10F and G). Similar results were observed for the combination of I-BRD9 and pomalidomide (Fig. 10H and I). These results improve the understanding of the correlation of BRD9 and neosubstrates in MM and may assist in the development of more effective therapeutic strategies involving synergy between BRD9 inhibitors and IMiDs for MM treatment.

Discussion

In this study, phenotypic profiling of a small molecule compounds library in multiple hematological cancer cell lines revealed that, a novel lead degrader with phthalazinone scaffold, **MGD-4**, exhibited submicromolar antiproliferative effects in MM and AML cells through CRBN-mediated degradation of IKZF1, IKZF2 and IKZF3. To enhance its potency and expand the range of neosubstrates that can be degraded, unbiased MD-based rational design, large cell-based identification, and unbiased proteomics were employed to obtain a novel potent degrader **MGD-28**, which exhibited significant efficacy against a broad range of hematological cancer cell lines with nanomolar IC_{50} values. In addition, **MGD-28** demonstrated nanomolar DC_{50} potency in degrading IKZF1/2/3 and CK1α, markedly exceeding the depth, kinetics, and potency of neosubstrate degradation induced by lenalidomide and pomalidomide. Single-agent oral administration of **MGD-28** and combination therapy with standard of care agents (dexamethasone, tazemetostat, and bortezomib) significantly inhibited the growth of MM xenograft. Moreover, **MGD-28** induced the degradation of other neosubstrates (e.g. ZFP91 and DTWD1) degradation and CRBN-dependent proteins degradation including ZNFX1, MBD1 and MDB3. Furthermore,

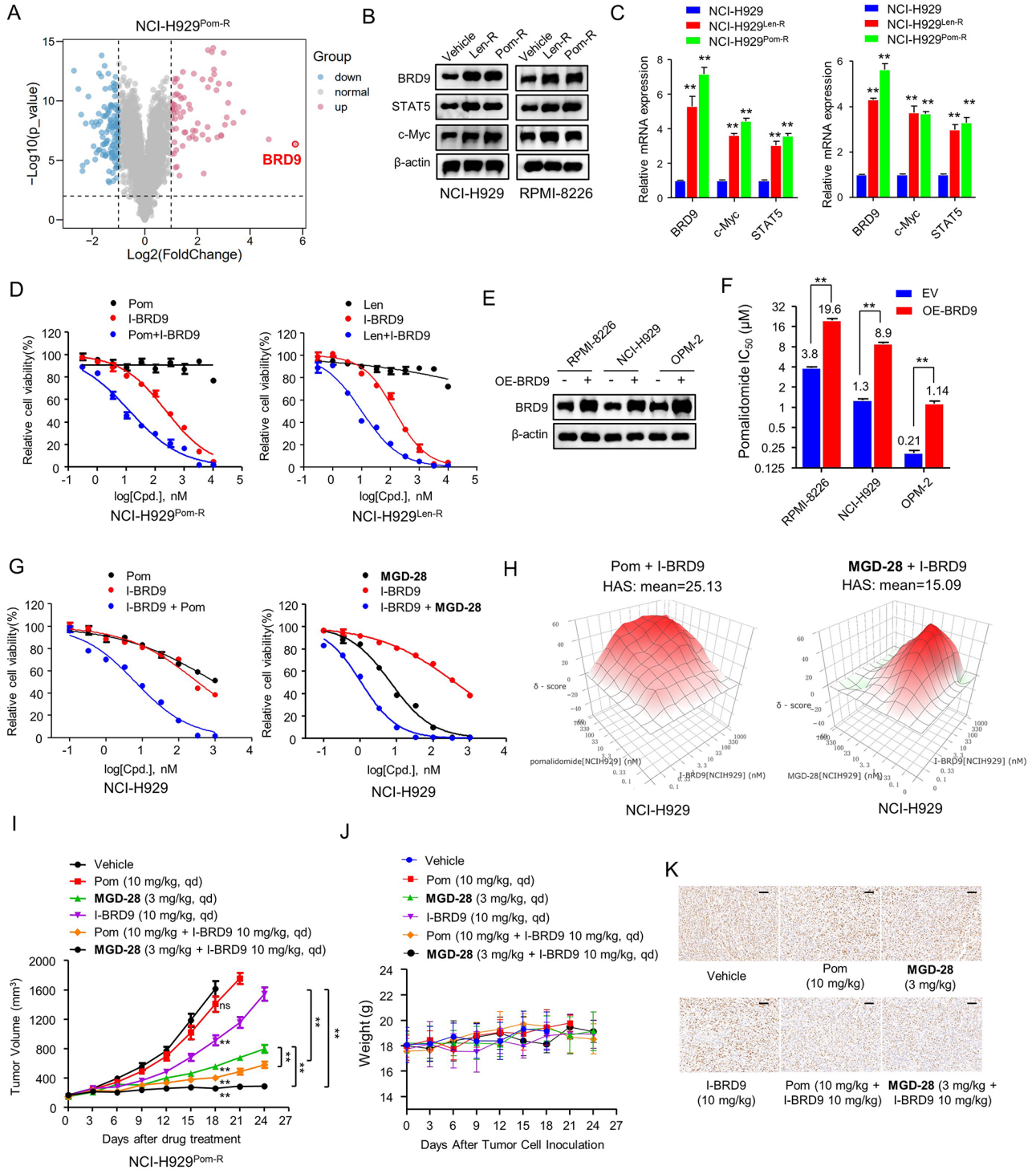

Fig. 9 (See legend on next page.)

MGD-28 exhibited preferential cytotoxic activity against MM cells compared with primary B cells as well as a broad antiproliferative profile against solid tumor cell lines, suggesting a wide range of potential therapeutic opportunities. Finally, through unbiased proteomics analysis of pomalidomide-/lenalidomide-resistant MM cells and cell-based functional assays, we demonstrated that BRD9 activation decreased the sensitivity MM cells to IMiDs, and BRD9 inhibition restored IMiDs-induced MM cytotoxicity and enhanced the effects of IMiDs against MM and AML. In clinical MM specimens, we

(See figure on previous page.)

Fig. 9 BRD9 activation mediates acquired resistance to IMiDs. **A.** Proteomics analysis of NCI-H929 cells that were resistant to pomalidomide (Pom-R). **B.** Western blot analysis of BRD9 in NCI-H929 and RPMI-8226 cells that were resistant to lenalidomide (Len-R) and pomalidomide (Pom-R), respectively. **C**. qPCR analysis of the indicated gene expression associated BRD9 in NCI-H929 and RPMI-8226 cells that were resistant to lenalidomide (Len-R) and pomalidomide (Pom-R), respectively, compared with parental NCI-H929 cells. Error bars denote standard deviations (independent experiments, $n = 3$). $^{**}p < 0.01$ (t-test). **D**. Effects of pomalidomide (Pom), lenalidomide (Len), I-BRD9 or drug combination on viability of NCI-H929 cells that were resistant to pomalidomide (NCI-H929^{Pom-R}, left) and lenalidomide (NCI-H929^{Len-R}, right), respectively. Data shown are a representative graph of three independent experiments; mean ± SD of triplicates. **E**-**F**. Effects of BRD9 overexpression on MM cell lines in response to pomalidomide treatment. WB analysis was conducted to detect BRD9 expression in MM cells that were stably transfected with empty vector (EV) or BRD9 (**E**). The effects of empty vector, BRD9 overexpression on the IC_{50} of pomalidomide are shown in the bar graph (**F**). Error bars denote standard deviations (independent experiments, $n = 3$). $^{**}p < 0.01$ (t-test). **G**. Effect of pomalidomide (Pom), **MGD-28**, I-BRD9 or drug combination on viability of NCI-H929 cells. Data shown are a representative graph of three independent experiments; mean ± SD of triplicates. **H**. Three-dimensional synergy score heatmaps for pomalidomide (Pom, left) or **MGD-28** (right) plus I-BRD9 combination in NCI-H929 cells calculated using SynergyFinder. **I**-**J**. NOD/SCID nude mice transplanted with NCI-H929^{Pom-R} cells were orally administrated with single agent I-BRD9, pomalidomide (Pom), **MGD-28** and vehicle as well as combinational treatment of I-BRD9 + Pom and I-BRD9 + **MGD-28** for 24 days. The change of NCI-H929^{Pom-R} tumor volume (**I**) and change of body weight (**J**) of all mice in each group were shown ($n = 7$). Data are mean ± SD, ns (no significance), $^{**}p < 0.01$ (one-way ANOVA). **K**. Representative images of Ki67-IHC staining in harvested tumors from each group in (**I**) are shown. Scale bars represent 50 mm

observed a positive correlation between BRD9 and CRBN at different MM stages.

CK1α has been identified as a potential target for hematological indications. However, classical ATP-competitive CK1α inhibitors, such as TG003, IC261, D4476, and epiblastin A, only exhibit submicromolar to micromolar IC_{50} inhibitory activity against CK1α with moderate antiproliferative efficacy, along with low subtype selectivity [17]. In contrast, CK1α degraders notably enhance pharmacodynamic activity both in vivo and in vitro, without inducing degradation of other CK1 protein subtypes. However, lenalidomide is the only drug approved by the FDA to induce CK1α protein degradation with moderate efficacy. This may explain why lenalidomide shows meaningful clinical effects in MDS characterized by CK1α haploinsufficiency, but lacks efficacy against AML in preclinical and clinical settings. Recently, the Gray and Woo labs reported the production of dual CK1α/IKZF2 degraders derived from lenalidomide [44]. Another study was conducted to optimize the substitution vector on lenalidomide to establish direct interactions with the degron motif, with the ultimate goal of developing selective CK1α degraders [22]. In this study, an IKZF1/2/3 degrader, **MGD-4**, with a novel phthalazinone structure, was discovered through phenotypic profiling as the lead compound. The structure of the compound was modified using MD based on the CK1α-IMiD-CRBN complex structure and mechanism of action, resulting in the identification of CK1α degraders (**MGD-15**, **MGD-18**, and **MGD-28**). The observed outstanding improvements can be rationalized by inducing CRBN^{Tyr355} residue inversion to enlarge the cavity of the β hairpin structure of CRBN, thus promoting the formation of stable ternary complexes induced by these degraders. In comparison, **MGD-15**, **MGD-18**, and **MGD-28** demonstrated superior CK1α degradation in terms of depth, kinetics, and potency relative to lenalidomide. The stability rank of the formed ternary complex directly reflects the trends observed in the degradation potency, validating our optimization strategy.

Multiple approaches have been used to improve the outcomes of patients resistant to IMiDs. Overall, the highly effective strategies can be classified into two categories. One is to continue targeting CRBN such as by exploring factors associated with CRBN, CRBN-binding proteins and CRL4^{CRBN} ligase or developing next-generation IMiD degraders to overcome resistance. The other is elucidating the underlying mechanisms of IMiDs-resistant state and exploiting combinational or synthetic lethality therapies. For the former, a previous study utilized CRISPR-Cas9 screening to identify genes that regulate the expression of CRBN to modulate IMiDs sensitivity [45]. Some studies exploited a series of newer generation of IMiDs, including CC-220 [46], CC-92,480 [47], and CFT7455 [48], which exhibit high binding affinity to CRBN and potent degradation efficacy on various neosubstrates, can overcome resistance to the earlier-generation of IMiDs such as thalidomide and pomalidomide. **MGD-28** demonstrated robust inhibitory effects with IC_{50} values ranging from double-digit nanomolar to submicromolar levels in lenalidomide-/pomalidomide-resistant MM cells. In addition, it exhibited antitumor activity in NCI-H929-pomalidomide resistant tumor growth in vivo. This effect may have resulted from its potent, rapid, and sustained degradation of IKZF1/2/3, CK1α or other significant reduced neosubstrates. Although downregulation or mutations in CRBN have been linked to IMiDs resistance, it is important to note that MM cells can exhibit resistance without CRBN dysfunction, suggesting the presence of alternative mechanisms of IMiDs resistance. For the latter, several novel pathways and their associated small molecule inhibitors have been investigated. Based on current data, the most promising avenues for further investigation may be those targeting the MEK pathway [49], extra-lineage transcription factors such as ETV4 [50], and epigenetic regulators such as CRBP/EP300 [51] and EZH2 [40, 52].

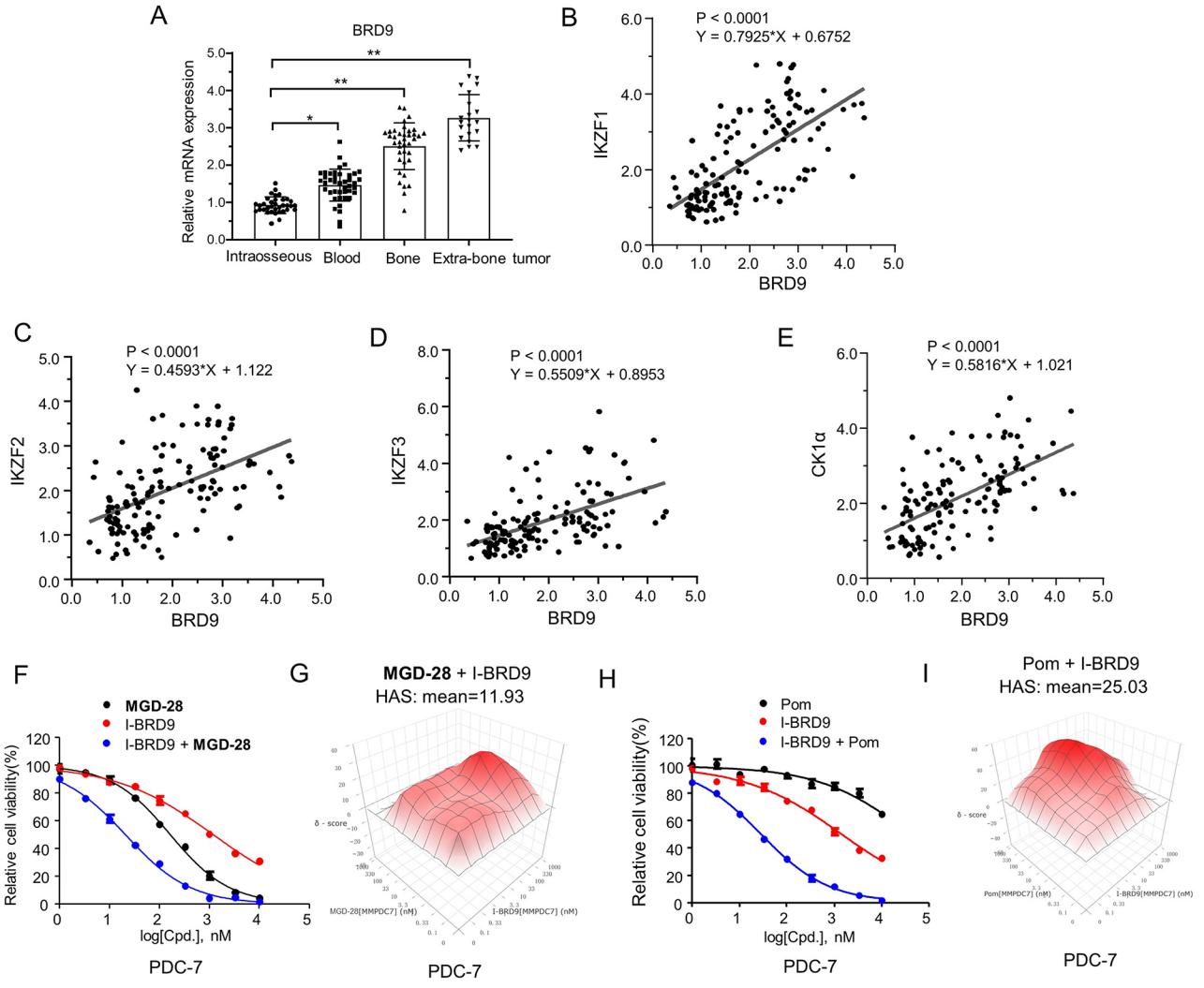

Fig. 10 Synergy between BRD9 inhibitors and IMiDs as a therapeutic strategy for MM. **A**. The expression level of BRD9 in MM specimens at different stages. * $p < 0.05$, ** $p < 0.01$. **B-E**. The association between BRD9 and IKZF1 (**B**), IKZF2 (**C**), IKZF3 (**D**) and CK1α (**E**) in MM specimens at different stages. **F**. Effect of **MGD-28**, I-BRD9 or drug combination on viability of PDC-7. Data shown are a representative graph of three independent experiments; mean ± SD of triplicates. **G**. Three-dimensional synergy score heatmaps for **MGD-28** plus I-BRD9 combination in PDC-7 calculated using SynergyFinder. **H**. Effect of pomalidomide (Pom), I-BRD9 or drug combination on viability of PDC-7. Data shown are a representative graph of three independent experiments; mean ± SD of triplicates. **I**. Three-dimensional synergy score heatmaps for pomalidomide (Pom) plus I-BRD9 combination in PDC-7 calculated using SynergyFinder

Our whole-proteome analysis of MM cells with acquired resistance to lenalidomide and pomalidomide revealed significant hyperactivation of BRD9 in both lenalidomide- and pomalidomide-resistant NCI-H929 cells. Previous studies have established BRD9 as a potential therapeutic target for certain sarcomas and leukemia. BRD9 tended to be highly expressed in patient MM cells compared with in normal plasma cells, and higher BRD9 expression was associated with poor overall survival [53]. Inhibition of BRD9 inhibits the growth and differentiation of AML cells [54], whereas degradation of BRD9 enhances the effects of several chemotherapeutic agents and targeted therapies against AML and MM [55]. Our findings indicate that overexpression of BRD9 conferred strong resistance in MM cells. In contrast, inhibition of BRD9 using I-BRD9 overcome resistance and mediates synergistic cytotoxicity with IMiDs in corresponding IMiD-resistant MM cells, both in vitro and in vivo. Moreover, analysis of MM specimens at different stages showed that higher BRD9 expression was associated with MM progression in patients with MM. Although BRD9 expression not positively related to CRBN at different disease stages of MM specimens (Fig. S10J), positive correlation between BRD9 with various neosubstrates (IKZF1, IKZF2, IKZF3, CK1α) was observed. These findings demonstrate the pivotal role of BRD9 in mediating IMiD resistance, and suggest that co-targeting BRD9 and

CRBN is a promising therapeutic approach against MM and AML.

Notably, the degradation mechanisms of IMiDs against a multitude of substrates enable their beneficial activities to be exerted in various contexts. To investigate the global protein degradation of neosubstrates induced by our degraders, we conducted quantitative proteomics. In addition to IKZF1 and CK1α, expression of ZFP91 and DTWD1 was significantly decreased in MM and AML cells following **MGD-4** and **MGD-28** treatment. Studies have demonstrated that ZFP91 is not only essential for the survival of bone marrow and B cell malignancies, but also synergizes with IKZF1 to regulate cell survival in IMiDs-resistant T cell lymphomas [56, 57]. These data suggest that use of **MGD-4**/**MGD-28** is be a promising therapeutic approach for patients with T-cell lymphomas patients. Furthermore, our findings indicate that **MGD-4** and **MGD-28** can induce CRBN-dependent ubiquitination and subsequent proteasomal degradation of ZNFX1, MBD1, and MBD3, and the protein level of them were increased during the co-immunoprecipitation with CRBN in the presence of **MGD-28**, pomalidomide, and CC-220, respectively. These results suggested that these proteins may act as IMiD-dependent $CRL4^{CRBN}$ substrates. ZNFX1 has been shown to activate intracellular immune pathways [58]. ZNFX1 antisense RNA 1, a novel long non-coding RNA transcribed in the antisense orientation of ZNFX1, is upregulated in multiple cancers, including gastric cancer and hepatocellular carcinoma, contributing to cancer development and progression [59]. However, the role of ZNFX1 in tumorigenesis remains to be elucidated. A substantial body of research has demonstrated the role of MBD1 and MBD3 in cancer development. High MBD1 expression is associated with lymph node metastasis and poor survival in patients with gallbladder cancer. MBD1 regulates epithelial-mesenchymal transition (EMT) program and is involved in resistance to gemcitabine chemotherapy [60]. MBD3 plays a pivotal role in multiple facets of the colon [61], gastric [62], and hepatocellular carcinomas [63], particularly the EMT process, which facilitates metastasis and leads to unfavorable prognoses. Furthermore, the levels of ZMIZ2 and MNT were significantly reduced by **MGD-4**/**MGD-28** treatment. ZMIZ2 is upregulated in triple negative breast cancer and promotes the progression of this cancer by stimulating CCL5, which affects several immune-related pathways, including NOD-like and Toll-like receptor signaling pathways [63]. MNT functions as a member of the MYC transcription factor network, suppresses MYC-driven apoptosis, and is essential for the survival of MYC-driven premalignant and malignant B lymphoid cells [64, 65]. Our findings indicate that patients with various malignancies harboring ZNFX1, MBD1, MBD3, ZMIZ2, and MNT may benefit from **MGD-4** and **MGD-28** treatment.

Despite these noteworthy findings, we acknowledge that there are still some imperfections in our study. First, the phenotypic screening approach relies solely on cell viability, which may overlook degraders that can serve as promising starting points for optimizing neosubstrate degradation. Moreover, because **MGD-28** shows a broad antiproliferative profile, studies are needed to investigate the effects of **MGD-28** as single agent or combined with other therapeutics in specific type of solid tumors. Furthermore, studies have demonstrated that IKZF2 is expressed in a majority of regulatory T cells, as well as in certain T cell and lymphocyte subsets [66], and IKZF2 depletion enhances the anti-tumor immune response in mouse syngeneic tumor models [67]. Thus, exploring the potential immunotherapeutic contribution of these degraders will reveal other promising therapies. Finally, although the homology between mouse CRBN and human CRBN is more than 97% and both mouse and human CRBN bind thalidomide derivatives, $CRBN^{Ile391}$ in murine causes steric hindrance that prevents recruitment of these neosubstrates and subsequent degradation in mice [68, 69], limiting investigation of their therapeutic activity or toxicity in vivo. **MGD-4** and **MGD-28** showed high specificity for tumor cells reflected by the minimal antiproliferative activity against primary B cells isolated from healthy individuals, however, a more relevant humanized mouse model (e.g., $CRBN^{I391V}$ mice) could be utilized to evaluate the toxicity and side effects of our degraders in preclinical studies.

Conclusion

This study offers a rationale for the application of **MGD-4** and **MGD-28** in a broad range of hematologic and solid tumor. Additionally, MD-based strategies are useful for rational optimization of CK1α degraders, Degrading IKZF1/2/3 and CK1α is a viable therapeutic strategy, providing a foundation for the development of other degraders with an expanded array of substrates to enhance their functionality and efficacy.

Abbreviations

IMiDs	IMmunomodulatory imide Drugs
MM	Multiple Myeloma
AML	Acute Myeloid Leukemia
DLBCL	Diffuse Large B Cell Lymphoma
PBMCs	Peripheral Blood Mononuclear Cells
CK1α	Casein Kinase 1α
MD	Molecular Dynamics
DC_{50}	Half-maximal Degradation Concentration
D_{max}	Maximal Degradation
PK	Pharmaco Kinetic
IHC	Immuno Histo Chemical
PDCs	Patient-Derived Cell lines
BRD9	BRomo Domain-containing protein 9
HAS	Highest Single-Agent
TGI	Tumor Growth Inhibition

Supplementary Information

The online version contains supplementary material available at https://doi.org/10.1186/s13045-024-01592-z.

Supplementary Material 1

Supplementary Material 2

Supplementary Material 3

Acknowledgements
We would like to thank Editage (www.editage.cn) for English language editing.

Author contributions
Zhibing Zheng, Junhai Xiao, Fan Feng, Xiaomei Zhuang and Song Li. conceived and directed the project. Zhibing Zheng, Pengyun Li, Xiaotong Hu, Fan Feng and Junhai Xiao contributed to experimental design and program strategy. Pengyun Li, Xiaotong Hu, Shiyang Sun, Jian Yan, Ning Yang, Changkai Jia, Tingting Yang and Xu Cai contributed to design and chemical synthesis of compounds. Pengyun Li, Zhiya Fan, Ting Wei, Pengli Wei, Qijie Ran, Qiyu Jiang, Tingting Xu, Yaqiu Mao. and Zhiyuan Zhao contributed to the in vitro biology experiments and data analysis. Pengyun Li, Xiaotong Hu, Ting Wei, Pengli Wei and Tingting Xu contributed to the in vivo biology experiments and data analysis. Pengyun Li, Xiaotong Hu, Zhiya Fan and Changkai Jia wrote the manuscript. Zhibing Zheng, Junhai Xiao, Fan Feng and Xiaomei Zhuang reviewed and edited the paper. Fan Feng, Qijie Ran and Qiyu Jiang contributed to the clinical MM patient specimens and correlation analysis. Xiaomei Zhuang contributed to the pharmacokinetic study in vivo and data analysis. All authors read and approved the final manuscript.

Funding
This study was supported by the State Key Laboratory of National Security Specially Needed Medicines Program (NO. LTMC2022ZZ006), National Natural Science Foundation of China (No. 32371504, 32088101 and 81702986).

Data availability
All data needed to evaluate the conclusions in the article are present in the article and/or the Supplementary Materials. The data and materials used in the current study are available from the corresponding authors upon reasonable request.

Declarations

Ethics approval and consent to participate
All animal studies were performed strictly in accordance with the Animal Care Guidelines approved by the Institutional Animal Care Committee of Beijing Institute of Biotechnology. The human related materials were included MM cells and tumor tissues, and the use of human experimental materials, including cDNA derived from cell lines and clinical specimens, have been reviewed and approved by Ethics Committee of the General Hospital of Central Theater Command. All the experiments using the human related materials were performed according to the Helsinki Declaration (WHO).

Consent for publication
Not applicable.

Competing interests
The authors declare no competing interests.

Author details
[1]National Engineering Research Center for Strategic Drugs, Beijing Institute of Pharmacology and Toxicology, Beijing 100850, China
[2]State Key Laboratory of National Security Specially Needed Medicines, Beijing Institute of Pharmacology and Toxicology, Beijing 100850, China
[3]State Key Laboratory of Medical Proteomics, Beijing Proteome Research Center, National Center for Protein Sciences (Beijing), Beijing Institute of Lifeomics, Beijing 102206, China
[4]Department of Clinical Laboratory, Fifth Medical Center of Chinese PLA General Hospital, Beijing 100039, China
[5]Department of Hematology, General Hospital of Central Theater Command, Wuhan 430012, China
[6]State Key Laboratory of Natural and Biomimetic Drugs, School of Pharmaceutical Sciences, Peking University, Beijing 100191, China

Received: 22 June 2024 / Accepted: 5 August 2024
Published online: 02 September 2024

References

1. Fuchs O. Targeting cereblon in hematologic malignancies. Blood Rev. 2023;57.
2. Maura F, Rajanna AR, Ziccheddu B, Poos AM, Derkach A, Maclachlan K, et al. Genomic classification and individualized prognosis in multiple myeloma. J Clin Oncol. 2024;42(11):1229–40.
3. van de Donk NWCJ, Pawlyn C, Yong KL. Multiple myeloma. Lancet. 2021;397(10272):410–27.
4. Yamamoto J, Ito T, Yamaguchi Y, Handa H. Discovery of CRBN as a target of thalidomide: a breakthrough for progress in the development of protein degraders. Chem Soc Rev. 2022;51(15):6234–50.
5. Lu G, Middleton RE, Sun H, Naniong M, Ott CJ, Mitsiades CS, et al. The myeloma drug lenalidomide promotes the cereblon-dependent destruction of Ikaros proteins. Science. 2014;343(6168):305–9.
6. Bjorklund CC, Lu L, Kang J, Hagner PR, Havens CG, Amatangelo M, et al. Rate of CRL4(CRBN) substrate ikaros and Aiolos degradation underlies differential activity of lenalidomide and pomalidomide in multiple myeloma cells by regulation of c-Myc and IRF4. Blood Cancer J. 2015;5(10):e354.
7. Kronke J, Fink EC, Hollenbach PW, MacBeth KJ, Hurst SN, Udeshi ND, et al. Lenalidomide induces ubiquitination and degradation of CK1alpha in Del(5q) MDS. Nature. 2015;523(7559):183–8.
8. An J, Ponthier CM, Sack R, Seebacher J, Stadler MB, Donovan KA et al. pSILAC mass spectrometry reveals ZFP91 as IMiD-dependent substrate of the CRL-4CRBN ubiquitin ligase. Nat Commun. 2017;8(1).
9. Matyskiela ME, Lu G, Ito T, Pagarigan B, Lu CC, Miller K, et al. A novel cereblon modulator recruits GSPT1 to the CRL4(CRBN) ubiquitin ligase. Nature. 2016;535(7611):252–7.
10. Donovan KA, An J, Nowak RP, Yuan JC, Fink EC, Berry BC, et al. Thalidomide promotes degradation of SALL4, a transcription factor implicated in Duane Radial Ray syndrome. eLife. 2018;7:e38430.
11. Matyskiela ME, Couto S, Zheng X, Lu G, Hui J, Stamp K, et al. SALL4 mediates teratogenicity as a thalidomide-dependent cereblon substrate. Nat Chem Biol. 2018;14(10):981–7.
12. Sievers QL, Petzold G, Bunker RD, Renneville A, Slabicki M, Liddicoat BJ et al. Defining the human C2H2 zinc finger degrome targeted by thalidomide analogs through CRBN. Science. 2018;362(6414).
13. Asatsuma-Okumura T, Ando H, De Simone M, Yamamoto J, Sato T, Shimizu N, et al. p63 is a cereblon substrate involved in thalidomide teratogenicity. Nat Chem Biol. 2019;15(11):1077–84.
14. Renneville A, Gasser JA, Grinshpun DE, Jean Beltran PM, Udeshi ND, Matyskiela ME, et al. Avadomide induces degradation of ZMYM2 Fusion oncoproteins in Hematologic malignancies. Blood Cancer Discov. 2021;2(3):250–65.
15. Carter JL, Hege K, Yang J, Kalpage HA, Su Y, Edwards H et al. Targeting multiple signaling pathways: the new approach to acute myeloid leukemia therapy. Signal Transduct Tar. 2020;5(1).
16. Cowan AJ, Green DJ, Kwok M, Lee S, Coffey DG, Holmberg LA, et al. Diagnosis and management of multiple myeloma: a review. JAMA. 2022;327(5):464–77.
17. Jiang S, Zhang M, Sun J, Yang X. Casein kinase 1α: biological mechanisms and theranostic potential. Cell Commun Signal. 2018;16(1).
18. Huart A-S, MacLaine N, Meek D, Hupp T. CK1 alpha plays a Central Role in Mediating MDM2 Control of p53 and E2F-1 protein Stability. J Biol Chem. 2009;284:32384–94.
19. Janovska P, Verner J, Kohoutek J, Bryjova L, Gregorova M, Dzimkova M, et al. Casein kinase 1 is a therapeutic target in chronic lymphocytic leukemia. Blood. 2018;131(11):1206–18.
20. Manni S, Carrino M, Piazza F. Role of protein kinases CK1α and CK2 in multiple myeloma: regulation of pivotal survival and stress-managing pathways. J Hematol Oncol. 2017;10(1).
21. Park S-M, Miyamoto DK, Han GYQ, Chan M, Curnutt NM, Tran NL, et al. Dual IKZF2 and CK1α degrader targets acute myeloid leukemia cells. Cancer Cell. 2023;41(4):726–e3911.

22. Nishiguchi G, Mascibroda LG, Young SM, Caine EA, Abdelhamed S, Kooijman JJ et al. Selective CK1α degraders exert antiproliferative activity against a broad range of human cancer cell lines. Nat Commun. 2024;15(1).
23. Gao S, Wang S, Song Y. Novel immunomodulatory drugs and neo-substrates. Biomark Res. 2020;8:2.
24. Yamanaka S, Horiuchi Y, Matsuoka S, Kido K, Nishino K, Maeno M, et al. A proximity biotinylation-based approach to identify protein-E3 ligase interactions induced by PROTACs and molecular glues. Nat Commun. 2022;13(1):183.
25. Ran Q, Xu D, Wang Q, Wang D. Hypermethylation of the promoter region of miR-23 enhances the metastasis and proliferation of multiple myeloma cells via the aberrant expression of uPA. Front Oncol. 2022;12:835299.
26. Chamberlain PP, Lopez-Girona A, Miller K, Carmel G, Pagarigan B, Chie-Leon B, et al. Structure of the human Cereblon-DDB1-lenalidomide complex reveals basis for responsiveness to thalidomide analogs. Nat Struct Mol Biol. 2014;21(9):803–9.
27. Sastry GM, Adzhigirey M, Day T, Annabhimoju R, Sherman W. Protein and ligand preparation: parameters, protocols, and influence on virtual screening enrichments. J Comput Aided Mol Des. 2013;27(3):221–34.
28. Shelley JC, Cholleti A, Frye LL, Greenwood JR, Timlin MR, Uchimaya M. Epik: a software program for pK(a) prediction and protonation state generation for drug-like molecules. J Comput Aided Mol Des. 2007;21(12):681–91.
29. Friesner RA, Murphy RB, Repasky MP, Frye LL, Greenwood JR, Halgren TA, et al. Extra precision glide: docking and scoring incorporating a model of hydrophobic enclosure for protein-ligand complexes. J Med Chem. 2006;49(21):6177–96.
30. Van Der Spoel D, Lindahl E, Hess B, Groenhof G, Mark AE, Berendsen HJ. GROMACS: fast, flexible, and free. J Comput Chem. 2005;26(16):1701–18.
31. Wang J, Wolf RM, Caldwell JW, Kollman PA, Case DA. Development and testing of a general amber force field. J Comput Chem. 2004;25(9):1157–74.
32. Case DA, Cheatham TE 3rd, Darden T, Gohlke H, Luo R, Merz KM Jr., et al. The Amber biomolecular simulation programs. J Comput Chem. 2005;26(16):1668–88.
33. Sousa da Silva AW, Vranken WF. ACPYPE - AnteChamber PYthon Parser interfacE. BMC Res Notes. 2012;5:367.
34. Maier JA, Martinez C, Kasavajhala K, Wickstrom L, Hauser KE, Simmerling C. ff14SB: improving the Accuracy of protein side chain and backbone parameters from ff99SB. J Chem Theory Comput. 2015;11(8):3696–713.
35. Springborg M, Kirtman B. Efficient vector potential method for calculating electronic and nuclear response of infinite periodic systems to finite electric fields. J Chem Phys. 2007;126(10):104107.
36. Ma J, Chen T, Wu S, Yang C, Bai M, Shu K, et al. iProX: an integrated proteome resource. Nucleic Acids Res. 2019;47(D1):D1211–7.
37. Chen T, Ma J, Liu Y, Chen Z, Xiao N, Lu Y, et al. iProX in 2021: connecting proteomics data sharing with big data. Nucleic Acids Res. 2022;50(D1):D1522–7.
38. Patil A, Manzano M, Gottwein E. CK1α and IRF4 are essential and independent effectors of immunomodulatory drugs in primary effusion lymphoma. Blood. 2018;132(6):577–86.
39. Rushworth SA, Bowles KM, Barrera LN, Murray MY, Zaitseva L, MacEwan DJ. BTK inhibitor ibrutinib is cytotoxic to myeloma and potently enhances bortezomib and lenalidomide activities through NF-κB. Cell Signal. 2013;25(1):106–12.
40. Li Y, Barber A, Martin S, Morales S, Bird S, Chrisochoidou Y, et al. EZH2 inhibition overcomes Immunomodulatory Drug (IMiD) Resistance in multiple myeloma cell lines in a Cereblon Pathway Dependent Manner. Blood. 2023;142(Supplement 1):4187.
41. Bushweller JH. Targeting transcription factors in cancer — from undruggable to reality. Nat Rev Cancer. 2019;19(11):611–24.
42. Wang Z-Q, Zhang Z-C, Wu Y-Y, Pi Y-N, Lou S-H, Liu T-B et al. Bromodomain and extraterminal (BET) proteins: biological functions, diseases, and targeted therapy. Signal Transduct Tar. 2023;8(1).
43. Zhu X, Liao Y, Tang L. Targeting BRD9 for Cancer Treatment: a New Strategy. OncoTargets Ther. 2020;13:13191–200.
44. Miyamoto DK, Curnutt NM, Park S-M, Stavropoulos A, Kharas MG, Woo CM. Design and development of IKZF2 and CK1α dual degraders. J Med Chem. 2023;66(24):16953–79.
45. Liu J, Song T, Zhou W, Xing L, Wang S, Ho M, et al. A genome-scale CRISPR-Cas9 screening in myeloma cells identifies regulators of immunomodulatory drug sensitivity. Leukemia. 2019;33(1):171–80.
46. Bjorklund CC, Kang J, Amatangelo M, Polonskaia A, Katz M, Chiu H, et al. Iberdomide (CC-220) is a potent cereblon E3 ligase modulator with antitumor and immunostimulatory activities in lenalidomide- and pomalidomide-resistant multiple myeloma cells with dysregulated CRBN. Leukemia. 2019;34(4):1197–201.
47. Hansen JD, Correa M, Nagy MA, Alexander M, Plantevin V, Grant V, et al. Discovery of CRBN E3 ligase modulator CC-92480 for the treatment of relapsed and refractory multiple myeloma. J Med Chem. 2020;63(13):6648–76.
48. Lonial S, Richard S, Matous J, Yee A, Shah U, Mehta-Shah N, et al. Pharmacokinetic (PK) profile of a novel IKZF1/3 degrader, CFT7455, enables significant potency advantage over other IKZF1/3 degraders in models of multiple myeloma (MM) and the results of the initial treatment cohort from a first-in-human (FIH) phase 1/2 study of CFT7455 in MM. Cancer Res. 2022;82:CT186–CT.
49. Liu J, Hideshima T, Xing L, Wang S, Zhou W, Samur MK, et al. ERK signaling mediates resistance to immunomodulatory drugs in the bone marrow microenvironment. Sci Adv. 2021;7(23):eabg2697.
50. Neri P, Tagoug I, Maity R, Stein CK, Kong M, Keats J, et al. Transcriptional plasticity compensates for Ikaros and Aiolos Proteasomal Degradation and mediates resistance to IMiDs in multiple myeloma (MM). Blood. 2017;130:63.
51. Zhu YX, Shi C-X, Bruins LA, Wang X, Riggs DL, Porter B et al. Identification of lenalidomide resistance pathways in myeloma and targeted resensitization using cereblon replacement, inhibition of STAT3 or targeting of IRF4. Blood Cancer J. 2019;9(2).
52. Dimopoulos K, Søgaard Helbo A, Fibiger Munch-Petersen H, Sjö L, Christensen J, Sommer Kristensen L, et al. Dual inhibition of DNMTs and EZH2 can overcome both intrinsic and acquired resistance of myeloma cells to IMiDs in a cereblon-independent manner. Mol Oncol. 2017;12(2):180–95.
53. Kurata K, Samur MK, Liow P, Wen K, Yamamoto L, Liu J, et al. BRD9 degradation disrupts Ribosome Biogenesis in multiple myeloma. Clin Cancer Res. 2023;29(9):1807–21.
54. Zhou L, Yao Q, Li H, Chen J. Targeting BRD9 by I-BRD9 efficiently inhibits growth of acute myeloid leukemia cells. Transl Cancer Res. 2021;10(7):3364–72.
55. Weisberg E, Chowdhury B, Meng C, Case AE, Ni W, Garg S et al. BRD9 degraders as chemosensitizers in acute leukemia and multiple myeloma. Blood Cancer J. 2022;12(7).
56. Mi C, Wang Z, Li MY, Zhang ZH, Ma J, Jin X. Zinc finger protein 91 positively regulates the production of IL-1β in macrophages by activation of MAPKs and non-canonical caspase-8 inflammasome. Brit J Pharmacol. 2018;175(23):4338–52.
57. Wu W, Nelson GM, Koch R, Donovan KA, Nowak RP, Heavican-Foral TB, et al. Overcoming IMiD resistance in T-cell lymphomas through potent degradation of ZFP91 and IKZF1. Blood. 2022;139(13):2024–37.
58. Wang Y, Yuan S, Jia X, Ge Y, Ling T, Nie M, et al. Mitochondria-localised ZNFX1 functions as a dsRNA sensor to initiate antiviral responses through MAVS. Nat Cell Biol. 2019;21(11):1346–56.
59. He A, He S, Li X, Zhou L. ZFAS1: a novel vital oncogenic lncRNA in multiple human cancers. Cell Prolif. 2018;52(1).
60. Wensheng L, Bo Z, Qiangsheng H, Wenyan X, Shunrong J, Jin X et al. MBD1 promotes the malignant behavior of gallbladder cancer cells and induces chemotherapeutic resistance to gemcitabine. Cancer Cell Int. 2019;19(1).
61. Ding Y, Wang H, Liu J, Jiang H, Gong A, Xu M. MBD3 as a potential biomarker for Colon cancer: implications for epithelial-mesenchymal transition (EMT) pathways. Cancers. 2023;15(12).
62. Wang H, Min J, Ding Y, Yu Z, Zhou Y, Wang S et al. MBD3 promotes epithelial-mesenchymal transition in gastric cancer cells by upregulating ACTG1 via the PI3K/AKT pathway. Biol Proced Online. 2024;26(1).
63. Yan W, Han Q, Gong L, Zhan X, Li W, Guo Z, et al. MBD3 promotes hepatocellular carcinoma progression and metastasis through negative regulation of tumour suppressor TFPI2. Brit J Cancer. 2022;127(4):612–23.
64. Nguyen HV, Vandenberg CJ, Ng AP, Robati MR, Anstee NS, Rimes J, et al. Development and survival of MYC-driven lymphomas require the MYC antagonist MNT to curb MYC-induced apoptosis. Blood. 2020;135(13):1019–31.
65. Nguyen HV, Vandenberg CJ, Robati MR, Ng AP, Cory S. MNT suppresses T cell apoptosis via BIM and is critical for T lymphomagenesis. Cell Death Differ. 2023;30(4):1018–32.
66. Thornton AM, Korty PE, Tran DQ, Wohlfert EA, Murray PE, Belkaid Y, et al. Expression of Helios, an Ikaros Transcription Factor Family Member, differentiates thymic-derived from peripherally Induced Foxp3 + T Regulatory cells. J Immunol. 2010;184(7):3433–41.
67. Nakagawa H, Sido JM, Reyes EE, Kiers V, Cantor H, Kim H-J. Instability of Helios-deficient Tregs is associated with conversion to a T-effector phenotype and enhanced antitumor immunity. P Natl Acad Sci USA. 2016;113(22):6248–53.

68. Petzold G, Fischer ES, Thomä NH. Structural basis of lenalidomide-induced CK1α degradation by the CRL4CRBN ubiquitin ligase. Nature. 2016;532(7597):127–30.
69. Fink EC, McConkey M, Adams DN, Haldar SD, Kennedy JA, Guirguis AA, et al. Crbnl391V is sufficient to confer in vivo sensitivity to thalidomide and its derivatives in mice. Blood. 2018;132(14):1535–44.

Publisher's Note